current during depolarizing and hyperpolarizing (–50 mV) steps, as previously reported [Bendahhou et al., 2005; Schroeder et al., 2000]. After the recordings of Q1 with or without E3 current, we applied HMR1556 (1 &muM), a selective Q1 channel blocker. Though the sensitivity on the Q1 alone and Q1+E3 channel of chromanol 293B, another Q1 channel blocker, was different [Bett et al., 2006], both Q1 and Q1+E3 currents were almost totally abolished by only 1 &muM HMR1556 (lower panels of Fig. 4A).

HMR1556-sensitive current densities at the end of test pulse (Fig. 4B) were averaged from data and are plotted as the function of test voltage of Q1 (closed square), Q1+E3-WT (closed circle), Q1+E3-R99λH (open triangle), Q1+E3-T4A (open circle), and Q1+E3-P39R (closed triangle). Currents reconstituted by Q1 alone were activated at potentials greater than –40 mV, whereas those by Q1+E3 (WT and all mutants) were active at all test potentials and exhibited a strong outward rectification with a reversal potential close to E_K (–84 mV as predicted by Nernst equation). All three E3 mutants, E3-R99λH, E3-T4A, and E3-P39R, produced membrane currents with properties qualitatively similar to those of E3-WT. As summarized in Figure 4C, the current densities for the Q1+E3-R99λH current at +40 and –120 mV were 163.7±26.3 and –10.1±2.6 pA/pF, respectively. These values were significantly smaller than those of the Q1+E3-WT (301.6±33.3 pA/pF at +40 mV and –24.5±4.2 pA/pF at –120 mV, $P<0.05$). Q1+E3-T4A and Q1+E3-P39R displayed no statistically significant difference. The deactivation time constant for tail currents was significantly decreased by coexpression of E3 with Q1, but these three mutations in E3 had no significant effect on deactivation kinetics (Fig. 4D).

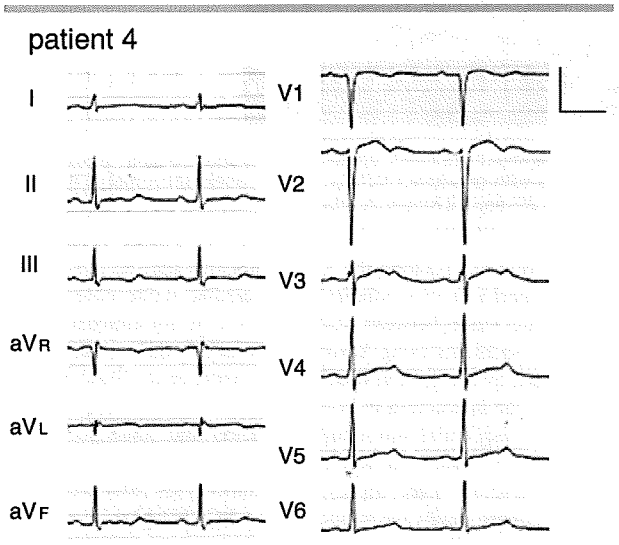

Figure 3. The 12-lead ECG of Patient 4 with QT prolongation. The patient was found to have a KCNE3-SNP, P39R, and a KCNH2-mutation, W536G.

Cellular Immunocytochemistry of KCNE3

It was reported that no E3 could be expressed on the plasma membrane in the absence of Q1 [Schroeder et al., 2000]. This was reconfirmed in our experimental protocol; the two left columns in Figure 5 show that HA-tagged E3 is not detected by Alexa 488 conjugated HA antibodies in nonpermeabilized COS7 cells in the

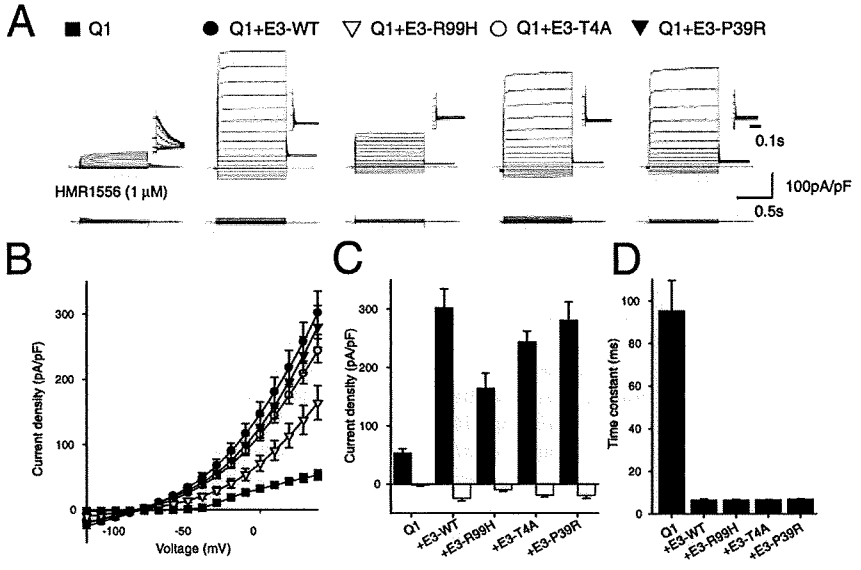

Figure 4. Functional analysis of KCNE3 and its mutants in a CHO cell line stably expressing KCNQ1 channel. **A:** Whole-cell membrane currents recorded from stable KCNQ1-CHO cells transfected without (Q1) or with KCNE3-wild type (Q1+E3-WT), KCNE3-R99λH (Q1+E3-R99λH), KCNE3-T4A (Q1+E3-T4A), or KCNE3-P39R (Q1+E3-P39R). Cells were held at –80 mV and stepped to various test potentials ranging from –120 to +40 mV in 10 mV steps for 1 sec before (upper panel) and during (lower panel) exposure to HMR1556 (1 μM). Dotted line indicates zero current level. Scale bars indicate 0.5 sec and 100 pA/pF. Insets to right of each recording illustrate expanded views of tail current elicited after return to –50 mV from test potentials. Scale bar indicates 0.1 sec. **B:** Current-voltage relationships for mean values of HMR1556-sensitive currents measured at the end of test pulses in CHO cells expressing Q1 (closed square, n = 5), Q1+E3-WT (closed circle, n = 14), Q1+E3-R99λH (open triangle, n = 12), Q1+E3-T4A (open circle, n = 12), or Q1+E3-P39R (closed triangle, n = 10). **C:** Summary of the current density measured at +40 (black bar) and –120 mV (white bar). Columns and error bars indicate mean±SEM. **D:** Deactivation time constant calculated by fitting a single exponential function to tail current at –50 mV after depolarization to +40 mV.

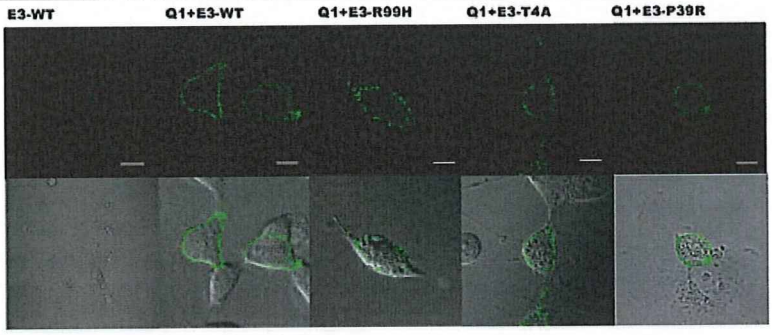

Figure 5. Cell surface expression of WT and mutant KCNE3 channels in nonpermeabilized cell. Upper panels of each column indicate HA-tagged KCNE3 (E3) (WT and three variants) with Alexa 488-conjugated antibodies with or without KCNQ1. Lower panels show merge of green fluorescence and light transmission images. Scale bars indicate 50 &mum in E3-WT and 10 &mum in others.

absence of Q1 cotransfection. In contrast, HA-tagged E3 could be visualized in the presence of Q1, which indicates that the Q1 protein is necessary for E3 to be successfully trafficked to the cell membrane. Q1 plus HA-tagged E3 channels generated currents similar to those of Q1 plus untagged E3 channels (data not shown). Figure 5 illustrates representative sets of confocal images. COS7 cells were transfected with tagged E3 (WT, T4A, and R99λH) and Q1. All Q1 plus HA-tagged E3 exhibited green fluorescence in the plasma membrane indicating that these channels were trafficked to the plasma membrane normally.

Discussion

In the present study, we report three E3 variants found in 485 LQTS probands. One of the two novel mutations, R99λH, displayed a significant decrease in outward currents when coexpressed with Q1. The proband with the E3-R99λH mutation suffered from drug-induced TdP. After washout of disopyramide, her QTc time on the ECG returned within normal range. The drug probably induced remarkable QT prolongation and TdP in the presence of a reduced repolarization reserve [Roden, 1998], which was associated with the E3-R99λH mutation.

The expression of E3 was confirmed in the human heart [Bendahhou et al., 2005; Lundquist et al., 2005, 2006]. Though neither the presence nor potential function of Q1+E3 channels in human cardiac myocytes have been determined, E3 conformed a functional channel in interaction with Q1, constitutively open potassium channel [Schroeder et al., 2000]. In addition, azimilide-sensitive Q1+E3 like currents were recorded in canine myocytes [Dun and Boyden, 2005]. On account of these results, E3 is assumed to have a physiological role in human heart. Mazhari et al. [2002] studied the effects of E3 on action potential duration (APD) in in vivo transduction of guinea pig ventricular myocytes. APD of E3-transduced myocytes was significantly reduced compared to that of control myocytes. Under the assumption that E3 might interact with KCNH2, they also performed a series of tests using an I_{Kr} blocker (E-4031) to determine whether the APD shortening was due to the interaction with E3 and KCNH2. However, E-4031 did not affect the APD in E3-transduced myocytes. As a result, the APD shortening appeared to be a result of the interaction between Q1 and E3. Although ventricular myocytes are repolarized mainly by Q1+E1 (I_{Ks}) and KCNH2 (I_{Kr}) in human hearts, we believe that the mutant E3 could prolong APD through interaction with Q1. We recently reported the knockdown of E3 expression using RNA interference in guinea pig ventricular myocytes [Toyoda et al., 2008]. The knockdown of E3 was found to prolong the APD, suggesting that E3 may play a physiological role in repolarization of cardiac action potential.

The interaction between KCNH2 and E3 is not established yet. In the experiments using *Xenopus* oocytes, KCNH2 currents were suppressed by coinjection with E3 [Schroeder et al., 2000]. On the contrary, the interaction in horse hearts could not be displayed by means of sequential immunoprecipitation and immunoblotting [Finley et al., 2002]. In addition, the I_{Kr} blocker did not affect APD in E3-transduced myocytes in guinea pigs [Mazhari et al., 2002]. Consequently, we supposed that KCNH2 plus E3 channel would affect very little for repolarization. We therefore did not pursue further examination on the interaction with KCNH2 and E3 using mammalian cell lines.

Regarding the E3-T4A mutation, we postulated that the E3-T4A has minor effects on the QT prolongation, based on the fact that no E3-T4A variant was found in our normal control. Though one of the probands had a *KCNH2*-G572S mutation [Tester et al., 2005] which is supposed to be the major reason for the QT prolongation, another proband had no mutation in major LQTS-related genes. In our biophysical assay, the mutant caused no significant difference in Q1+E3-T4A channel currents; therefore we could not display the association between E3-T4A mutation and QT prolongation. In patient 3, hypokalemia triggered the TdP, accordingly reducing extracellular potassium level may affect the currents through Q1+E3-T4A channels. Or E3 may also interact with another potassium channel alpha-subunit that affects the repolarization of cardiac myocytes, and the E3-T4A mutation may decrease the outward current to prolong QT time. We have to take into account that E3-T4A is a rare SNP, because the correlation between phenotype and genotype in our patients was not common and the number of our control was smaller compared to the studied cases.

E3-P39R may also have functional effects on repolarization. However, our proband with E3-P39R had a compound *KCNH2*-W563G mutation, as well as typical symptoms and ECG findings (Fig. 3) compatible with type 2 LQTS. In addition, functional analysis of the Q1+E3-P39R channel displayed smaller current densities than those of the Q1+E3-WT channel; however there was no statistical difference. Therefore we considered E3-P39R as a rare normal variant in Japanese.

Concerning another α subunit which interacts with KCNE3, Kv4.3 potassium channel encoded by *KCND3* produces transient outward potassium conductance (I_{to}) in the heart and KCNE3 inhibits the Kv4.3 currents [Lundby and Olesen, 2006; Radicke et al., 2006], even in the presence of KChIP2. Hence, there is a possibility that our E3 mutants affect the Kv4.3 current and prolong QT interval.

In conclusion, we identified three E3 variants among 485 Japanese LQTS probands, and one of which significantly reduced currents by interacting with Q1. Though the proband had remained asymptomatic in the absence of risk predisposing to QT prolongation, she fell into highly critical condition by taking disopyramide for AF at age of 76. Therefore, identification of E3 mutations with possible phenotypic effects provides us with information for our understanding of the mechanism of LQTS.

Acknowledgments

We thank the Japanese LQT families for their willingness to participate in this study. We are grateful to Ms. Arisa Ikeda for providing expert technical assistance, and we thank Dr. Takahiro Mitsueda for phenotypic data collection and Mr. Richard Kaszynski for reading the manuscript. W.S., Y.M., and M.H. were supported by a Health Sciences Research grant (H18-Research on Human Genome-002) from the Ministry of Health, Labour and Welfare, Japan.

References

Abbott GW, Sesti F, Splawski I, Buck ME, Lehmann MH, Timothy KW, Keating MT, Goldstein SA. 1999. MiRP1 forms I_{Kr} potassium channels with HERG and is associated with cardiac arrhythmia. Cell 97:175–187.

Abbott GW, Butler MH, Bendahhou S, Dalakas MC, Ptacek LJ, Goldstein SA. 2001. MiRP2 forms potassium channels in skeletal muscle with Kv3.4 and is associated with periodic paralysis. Cell 104:217–231.

Bendahhou S, Marionneau C, Haurogne K, Larroque MM, Derand R, Szuts V, Escande D, Demolombe S, Barhanin J. 2005. In vitro molecular interactions and distribution of KCNE family with KCNQ1 in the human heart. Cardiovasc Res 67:529–538.

Bett GC, Morales MJ, Beahm DL, Duffey ME, Rasmusson RL. 2006. Ancillary subunits and stimulation frequency determine the potency of chromanol 293B block of the KCNQ1 potassium channel. J Physiol 576(Pt 3):755–767.

Dun W, Boyden PA. 2005. Diverse phenotypes of outward currents in cells that have survived in the 5-day-infarcted heart. Am J Physiol Heart Circ Physiol 289:H667–H673.

Finley MR, Li Y, Hua F, Lillich J, Mitchell KE, Ganta S, Gilmour RF, Jr, Freeman LC. 2002. Expression and coassociation of ERG1, KCNQ1, and KCNE1 potassium channel proteins in horse heart. Am J Physiol Heart Circ Physiol 283:H126–H138.

Lundby A, Olesen SP. 2006. KCNE3 is an inhibitory subunit of the Kv4.3 potassium channel. Biochem Biophys Res Commun 346:958–967.

Lundby A, Ravn LS, Svendsen JH, Hauns S, Olesen SP, Schmitt N. 2008. KCNE3 mutation V17λM identified in a patient with lone atrial fibrillation. Cell Physiol Biochem 21:47–54.

Lundquist AL, Manderfield LJ, Vanoye CG, Rogers CS, Donahue BS, Chang PA, Drinkwater DC, Murray KT, George AL, Jr. 2005. Expression of multiple KCNE genes in human heart may enable variable modulation of I_{Ks}. J Mol Cell Cardiol 38:277–287.

Lundquist AL, Turner CL, Ballester LY, George AL, Jr. 2006. Expression and transcriptional control of human KCNE genes. Genomics 87:119–128.

Mazhari R, Nuss HB, Armoundas AA, Winslow RL, Marban E. 2002. Ectopic expression of KCNE3 accelerates cardiac repolarization and abbreviates the QT interval. J Clin Invest 109:1083–1090.

Morin TJ, Kobertz WR. 2007. A derivatized scorpion toxin reveals the functional output of heteromeric KCNQ1-KCNE K^+ channel complexes. ACS Chem Biol 2:469–473.

Moss AJ, Kass RS. 2005. Long QT syndrome: from channels to cardiac arrhythmias. J Clin Invest 115:2018–2024.

Ohno S, Zankov DP, Yoshida H, Tsuji K, Makiyama T, Itoh H, Akao M, Hancox JC, Kita T, Horie M. 2007. N- and C-terminal KCNE1 mutations cause distinct phenotypes of long QT syndrome. Heart Rhythm 4:332–340.

Radicke S, Cotella D, Graf EM, Banse U, Jost N, Varro A, Tseng GN, Ravens U, Wettwer E. 2006. Functional modulation of the transient outward current Ito by KCNE beta-subunits and regional distribution in human non-failing and failing hearts. Cardiovasc Res 71:695–703.

Roden DM. 1998. Taking the "idio" out of "idiosyncratic": predicting torsades de pointes. Pacing Clin Electrophysiol 21:1029–1034.

Schroeder BC, Waldegger S, Fehr S, Bleich M, Warth R, Greger R, Jentsch TJ. 2000. A constitutively open potassium channel formed by KCNQ1 and KCNE3. Nature 403:196–199.

Tester DJ, Will ML, Haglund CM, Ackerman MJ. 2005. Compendium of cardiac channel mutations in 541 consecutive unrelated patients referred for long QT syndrome genetic testing. Heart Rhythm 2:507–517.

Toyoda F, Ueyama H, Ding WG, Matsuura H. 2006. Modulation of functional properties of KCNQ1 channel by association of KCNE1 and KCNE2. Biochem Biophys Res Commun 344:814–820.

Toyoda F, Zankov DP, Ding WG, Matsuura H. 2008. Functional regulation of cardiac KCNQ1 potassium channel by association of KCNE3. [Abstract]. 2008 Biophysics Society Meeting Abstracts, February 2–6, 2008. Biophys J 94(Suppl):3025.

Comput Mech
DOI 10.1007/s00466-009-0432-1

ORIGINAL PAPER

Study of efficient homogenization algorithms for nonlinear problems

Approximation of a homogenized tangent stiffness to reduce computational cost

Jun-ichi Okada · Takumi Washio · Toshiaki Hisada

Received: 30 January 2009 / Accepted: 10 October 2009

Abstract A framework for the homogenization of nonlinear problems is discussed with respect to block LU factorization of the micro–macro coupled equation, and based on the relation between the characteristic deformation and the Schur-Complement as the homogenized tangent stiffness. In addition, a couple of approximation methods are introduced to reduce the computational cost, i.e., a simple scheme to reuse the old characteristic deformation and a sophisticated method based on the mode-superposition method developed by our group. Note that these approximation methods satisfy the equilibrium conditions in both scales. Then, using a simplified FE model, the conventional algorithm, a relative algorithm originating from the block LU factorization, and the above-mentioned algorithms with the approximated Schur-Complement are compared and discussed. Finally, a large-scale heart simulation using parallel computation is presented, based on the proposed method.

Keywords Homogenization method · Nonlinear finite element analysis · Schur-Complement · Mode superposition · Parallel computation · Block LU factorization · Heart

List of symbols

$\mathbf{Y}, \mathbf{y}$	Position vector around the deformation in the microstructure
$\mathbf{X}, \mathbf{x}$	Position vector around the deformation in the macrostructure
$\mathbf{u}$	Macroscopic displacement vector
$\{\mathbf{u}\}$	Macroscopic structure nodal displacement vector
$\{\mathbf{u}^e\}$	Macroscopic structure nodal displacement vector per element
$\mathbf{w}$	Periodic component of the microscopic displacement vector
$\{\mathbf{w}\}$	Periodic component of the nodal displacement vectors of all microstructures
$\{\mathbf{w}^Q\}$	Periodic component of the nodal displacement vector of a single microstructure
$\{\mathbf{w}^e\}$	Periodic component of the nodal displacement vector per element
$\mathbf{F}$	The deformation gradient tensor
$\mathbf{Z}$	The displacement gradient tensor
$\mathbf{C}$	The right Cauchy–Green tensor
$\mathbf{E}$	The Green–Lagrange strain tensor
$\mathbf{\Pi}$	The first Piola–Kirchhoff stress tensor
$\mathbf{I}$	The identity tensor
I_c, II_c, III_c	Principal invariants
J	Determinant $\mathbf{F}$

1 Introduction

The door to petaflop computing has recently opened and meaningful applications for massively parallel computers are being sought. A multi-scale approach to biomechanical problems is consequential in the post-genome era and the homogenization method is going to play a more important role than ever before. The homogenization method is a mathematical modeling technique for efficiently analyzing inhomogeneous material with a periodic microstructure. In

J. Okada (✉) · T. Washio · T. Hisada
Graduate School of Frontier Sciences, University of Tokyo,
5-1-5 Kashiwanoha, Kashiwa, Chiba 277-8563, Japan
e-mail: okada@sml.k.u-tokyo.ac.jp

Published online: 31 October 2009

biomaterial, the periodicity hypothesized in the homogenization method is not strictly established. However, Terada et al. [1] have shown that an appropriate equivalent characteristic is obtained in material with an irregular microstructure by assuming a periodic boundary condition. Thus, it is possible to evaluate the effect of each component in the microstructure on the macroscopic behavior, if microstructure modeling is appropriate. The homogenization method for biomaterial was applied to bone by Hollister and Kikuchi [2], while a two-dimensional analysis of engineered tissue cells was conducted by Breuls et al. [3]. In an example using the heart, Krassowska et al. [4] applied the method to an excitation propagation phenomena. To investigate the effect of intracellular structure on heartbeat, the authors have developed the necessary finite element homogenization method, where the heart is the macrostructure and the cardiomyocyte the microstructure. Thus the problem inevitably becomes a large-scale one.

In the homogenization method two scales are introduced, namely, a scale for the unit period, and a scale for the whole material. By solving the governing equations for both scales with coupling, we can obtain the macroscopic characteristic as an equivalent homogeneous body and variable distribution from the microstructure. In the conventional nonlinear homogenization method [5,6], it is first necessary to calculate microscopic equilibrium and then the macroscopic tangential homogenization updates all quadrature points at every Newton–Raphson iteration, resulting in huge computational cost. Even with a high performance computer, the cost is prohibitive for practical large-scale problems. To reduce this computational cost, various techniques have been devised. These include, for example, the construction of a database with the homogenized properties [7], sensitivity analysis [8], Fast Fourier Transforms [9], and so on. In a previous work, we proposed a homogenization method using characteristic deformation mode superposition [10,11]. This is, however, an approximation method and the accuracy depends on the problem. We subsequently proposed a new algorithm that solves the microscopic equilibrium equation alternately with the solution of the mode superposition-based micro–macro coupled equation. In this algorithm, the equilibrium conditions for both the micro and macro structures are satisfied with far less computational cost. This method is applicable to microstructures composed of slightly incompressible and viscoelastic materials [12–15].

Looking at this method from the block LU factorization of the micro–macro coupled equation, we recognize that the Schur-Complement as the homogenized tangent stiffness, is ingeniously approximated with the aid of mode superposition. It is further beneficial to generalize this view, that is, to interpret the framework of the homogenization method with regard to the block LU factorization and investigate how the Schur-Complement can be approximated to reduce the computational cost whilst preserving the accuracy. Accordingly, a couple of approximation methods, i.e., a simple scheme to reuse the old characteristic deformation and the above-mentioned mode-superposition based method, are introduced in this paper. Then a simplified numerical example is solved using both the conventional homogenization algorithm and the algorithm originating from the block LU factorization, and the performance of each is discussed. Finally, a large-scale heart simulation using parallel computation is presented based on the proposed method.

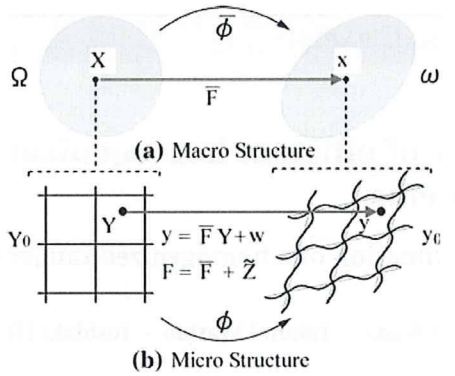

Fig. 1 Homogenization method for large deformation problems. **a** Macro structure. **b** Micro structure

2 Homogenization method for finite deformation problem

2.1 Problem statement and geometric prospect

We assume that the material in the body (Ω) reveals heterogeneity on a very fine scale and is characterized by the periodic distribution of a basic structural element (Y_0) as shown in Fig. 1. To measure the changes in the spatial domains, we introduce two scales: a macro-scale $X \in \Omega$ and a micro-scale $Y \in Y_0$. Thus the actual domain can be regarded as the product space ($\Omega \times Y_0$). In the subsequent development, the macroscopic quantity corresponding to the microscopic one is expressed with a bar symbol over the microscopic symbol. The following assumptions of homogenization are applied in the formulation of the homogenization method.

- A macrostructure that consists of a periodic microstructure can be considered to be an approximately equivalent homogeneous substance.
- A microstructure is infinitely fine compared with a macrostructure; the variable defined at each point of the macrostructure corresponds to the volume average of the variables in the microstructure.

It is assumed that the deformation of the microstructure is linked to the local values of the macro continuum via

$$\mathbf{y} = \overline{\mathbf{F}}\mathbf{Y} + \mathbf{w}, \tag{1}$$

where $\mathbf{y}$ and $\mathbf{Y}$ are position vectors defined on the microstructure [16].

The deformation consists of a homogeneous part $\overline{\mathbf{F}}\mathbf{Y}$ and a non-homogeneous superposed field $\mathbf{w}$. Consequently, the following relationships exist between the microscopic and macroscopic deformation gradients.

$$\mathbf{F} = \nabla_Y \mathbf{y} = \frac{\partial \mathbf{y}}{\partial \mathbf{Y}} = \overline{\mathbf{F}} + \tilde{\mathbf{Z}}, \tag{2}$$

$$\overline{\mathbf{F}} = \nabla_X \mathbf{x} = \frac{\partial \mathbf{x}}{\partial \mathbf{X}}, \tag{3}$$

$$\tilde{\mathbf{Z}} = \nabla_Y \mathbf{w} = \frac{\partial \mathbf{w}}{\partial \mathbf{Y}}. \tag{4}$$

Thus increment and variation of the deformation gradients are represented, respectively, as

$$\Delta\mathbf{F} = \Delta\overline{\mathbf{F}} + \Delta\tilde{\mathbf{Z}} = \Delta\overline{\mathbf{F}} + \nabla_Y \Delta\mathbf{w}, \tag{5}$$

$$\delta\mathbf{F} = \delta\overline{\mathbf{F}} + \delta\tilde{\mathbf{Z}} = \delta\overline{\mathbf{F}} + \nabla_Y \delta\mathbf{w}. \tag{6}$$

For the assumptions mentioned above, the macroscopic gradients are related via the volume averages

$$\overline{\mathbf{F}} = \frac{1}{|V|}\int_{Y_0} \mathbf{F} dY = \frac{1}{|V|}\int_{Y_0} (\overline{\mathbf{F}} + \tilde{\mathbf{Z}}) dY = \overline{\mathbf{F}} + \frac{1}{|V|}\int_{Y_0} \tilde{\mathbf{Z}} dY, \tag{7}$$

where V is the volume of the microstructure Y_0. Then, the fluctuation field $\mathbf{w}$ must satisfy the constraint

$$\int_{Y_0} \tilde{\mathbf{Z}} dY = \int_{Y_0} \frac{\partial \mathbf{w}}{\partial \mathbf{Y}} dY = \int_{\partial Y_0} \mathbf{N} \otimes \mathbf{w} dS = \mathbf{0}, \tag{8}$$

where $\mathbf{N}$ is an outward normal vector on the boundary ∂Y_0. This constraint is satisfied when $\mathbf{w}$ is periodic.

2.2 Formulation of homogenization method and finite element discretization

We now consider the equilibrium of material with a periodic microstructure, modeled by hyperelastic material. Using the principle of stationary potential energy, the equilibrium condition becomes a functional stationary problem. Under the homogenization assumptions, the macroscopic potential energy is related via the volume averages of the microscopic ones and the entire potential energy is defined by

$$\Phi = \int_\Omega \frac{1}{|V|}\int_{Y_0} W dY dX - \int_{\partial\Omega} \mathbf{t} \cdot \mathbf{u} dS, \tag{9}$$

where W is the strain energy function of the microstructure defined by the deformation gradient $\mathbf{F}$, and assuming conservative tractions. The stationary condition becomes

$$\delta\Phi = \int_\Omega \frac{1}{|V|}\int_{Y_0} \delta\mathbf{F} : \mathbf{\Pi} dY dX - F_{ext}(\delta\mathbf{u}) = 0, \tag{10}$$

$$\mathbf{\Pi} = \frac{\partial W}{\partial \mathbf{F}}, \tag{11}$$

$$F_{ext}(\delta\mathbf{u}) = \int_{\partial\Omega} \mathbf{t} \cdot \delta\mathbf{u} dS. \tag{12}$$

A similar equation has been reported by Terada and Kikuchi [5] using two-scale convergence theory [17]. We have also shown a formulation based on the mixed variational principle with a perturbed Lagrange-multiplier [14]. By inserting Eq. (6) into Eq. (10), macro and micro equilibrium equations can be derived based on the defined space of the variation.

$$\overline{G} = \int_\Omega \frac{1}{|V|}\int_{Y_0} \delta\overline{\mathbf{F}} : \mathbf{\Pi} dY dX - F_{ext}(\delta\mathbf{u}) = 0, \tag{13}$$

$$G = \int_{Y_0} \delta\tilde{\mathbf{Z}} : \mathbf{\Pi} dY = 0, \tag{14}$$

which achieves equilibrium under the given boundary condition in the macrostructure and self-equilibrium under a periodic boundary condition, Eq. (8), of the microscopic displacement in the microstructure. Thus the homogenization method simultaneously satisfies the two equilibrium conditions as described above. To solve the nonlinear equation, the Newton–Raphson method is employed. Then the standard linearization process in nonlinear finite element method provides the following linearized equations

$$\int_\Omega \frac{1}{|V|}\int_{Y_0} \delta\mathbf{F} : \mathbf{A} : \Delta\mathbf{F} dY dX = F_{ext}(\delta\mathbf{u}) - \int_\Omega \frac{1}{|V|}\int_{Y_0} \delta\mathbf{F} : \mathbf{\Pi} dY dX, \tag{15}$$

$$\mathbf{A} = \frac{\partial \mathbf{\Pi}}{\partial \mathbf{F}}. \tag{16}$$

Substituting Eqs. (5) and (6) into the above equation yields

$$\int_\Omega \frac{1}{|V|}\int_{Y_0} s(\delta\overline{\mathbf{F}} + \delta\tilde{\mathbf{Z}}) : \mathbf{A} : (\Delta\overline{\mathbf{F}} + \Delta\tilde{\mathbf{Z}}) dY dX = F_{ext}(\delta\mathbf{u}) - \int_\Omega \frac{1}{|V|}\int_{Y_0} (\delta\overline{\mathbf{F}} + \delta\tilde{\mathbf{Z}}) : \mathbf{\Pi} dY dX. \tag{17}$$

By finite element discretization using

$$\Delta\overline{\mathbf{F}} = [\overline{B^e}]\{\Delta\mathbf{u}^e\}, \tag{18}$$

$$\Delta\tilde{\mathbf{Z}} = [B^e]\{\Delta\mathbf{w}^e\}, \tag{19}$$

where $[B^e]$ is a shape function matrix, the left-hand side of Eq. (17) becomes

$$\begin{aligned}
&\{\delta \mathbf{w}^Q\}\frac{1}{|V|}\int_{Y_0}[B^e]^T[A][B^e]dY\{\Delta \mathbf{w}^Q\} \\
&\quad+\{\delta \mathbf{w}^Q\}\frac{1}{|V|}\int_{Y_0}[B^e]^T[A]dY[\overline{B^e}]\{\Delta \mathbf{u}^e\} \\
&\quad+\{\delta \mathbf{u}^e\}[\overline{B^e}]^T\frac{1}{|V|}\int_{Y_0}[A][B^e]dY\{\Delta \mathbf{w}^Q\} \\
&\quad+\{\delta \mathbf{u}^e\}[\overline{B^e}]^T\frac{1}{|V|}\int_{Y_0}[A]dY[\overline{B^e}]\{\Delta \mathbf{u}^e\} \\
&=\{\delta \mathbf{w}^Q\}\mathbf{K}^Q_{ww}\{\Delta \mathbf{w}^Q\}+\{\delta \mathbf{w}^Q\}\mathbf{K}^Q_{wu}\{\Delta \mathbf{u}^e\} \\
&\quad+\{\delta \mathbf{u}^e\}\mathbf{K}^Q_{uw}\{\Delta \mathbf{w}^Q\}+\{\delta \mathbf{u}^e\}\mathbf{K}^Q_{uu}\{\Delta \mathbf{u}^e\},
\end{aligned} \tag{20}$$

while the second term of the right-hand side of Eq. (17) becomes

$$-\{\delta \mathbf{u}^e\}[\overline{B^e}]^T\frac{1}{|V|}\int_{Y_0}[\Pi]dY-\{\delta \mathbf{w}^Q\}\frac{1}{|V|}\int_{Y_0}[B^e]^T[\Pi]dY, \tag{21}$$

at each quadrature point of the macrostructure. Symbol Q denotes the quantity that is evaluated at a macroscopic quadrature point, while symbol e denotes the quantity evaluated in the macroscopic element. By assembling these appropriately on the macro continuum, and considering the facultative variations, the following semi-positive definite symmetric matrix is obtained

$$\begin{bmatrix}\mathbf{K}_{ww} & \mathbf{K}_{wu}\\ \mathbf{K}_{uw} & \mathbf{K}_{uu}\end{bmatrix}\begin{Bmatrix}\Delta \mathbf{w}\\ \Delta \mathbf{u}\end{Bmatrix}=\begin{Bmatrix}\mathbf{r}_w\\ \mathbf{r}_u\end{Bmatrix}, \tag{22}$$

where

$$\mathbf{K}_{ww}=\int_\Omega\left(\frac{1}{|V|}\int_{Y_0}[B^e]^T[A][B^e]dY\right)dX \tag{23}$$

$$\mathbf{K}_{wu}=\int_\Omega\left(\frac{1}{|V|}\int_{Y_0}[B^e]^T[A]dY\right)[\overline{B^e}]dX \tag{24}$$

$$\mathbf{K}_{uw}=\int_\Omega[\overline{B^e}]^T\left(\frac{1}{|V|}\int_{Y_0}[A][B^e]dY\right)dX \tag{25}$$

$$\mathbf{K}_{uu}=\int_\Omega[\overline{B^e}]^T\left(\frac{1}{|V|}\int_{Y_0}[A]dY\right)[\overline{B^e}]dX \tag{26}$$

$$\{\mathbf{r}_w\}=-\int_\Omega\left(\frac{1}{|V|}\int_{Y_0}[B^e]^T[\Pi]dY\right)dX \tag{27}$$

$$\{\mathbf{r}_u\}=F_{ext}-\int_\Omega[\overline{B^e}]^T\left(\frac{1}{|V|}\int_{Y_0}[\Pi]dY\right)dX. \tag{28}$$

The nonlinear homogenization method solves Eq. (22) for $\Delta\mathbf{u}$ and $\Delta\mathbf{w}$ under the given boundary condition for the macrostructure and the periodic boundary condition (Eq. 8) for microscopic displacement. The number of degrees of freedom (NDOF) of this matrix is (NDOF of macrostructure + quadrature point of macrostructure × NDOF of microstructure). An enormous computational cost is, however, required to solve a small-scale problem. Moreover, it is difficult to solve the form given in Eq. (8) due to memory limitations, and generally, a transformation into the weak form takes place as described below.

2.3 Characteristic deformation

In a nonlinear problem, to evaluate the response of a microstructure to macroscopic deformation in a similar way to that in a linear problem [18], we obtain the following equation by taking the derivative of Eq. (14) at each quadrature point and substituting Eqs. (5) and (16).

$$\int_{Y_0}\delta\tilde{\mathbf{Z}}:\mathbf{A}:d\tilde{\mathbf{Z}}dY=-\int_{Y_0}\delta\tilde{\mathbf{Z}}:\mathbf{A}:d\overline{\mathbf{F}}dY \tag{29}$$

Since the macroscopic deformation gradient is independent of the microscopic integration,

$$\int_{Y_0}\delta\tilde{\mathbf{Z}}:\mathbf{A}:\frac{\partial\tilde{\mathbf{Z}}}{\partial\overline{\mathbf{F}}}dY=-\int_{Y_0}\delta\tilde{\mathbf{Z}}:\mathbf{A}:\mathbf{I}dY, \tag{30}$$

where $\mathbf{I}$ is a fourth order identity tensor, and the microstructural response of the macroscopic deformation gradient becomes

$$\frac{\partial\tilde{\mathbf{Z}}}{\partial\overline{\mathbf{F}}}=\nabla_Y\left(\frac{\partial\mathbf{w}}{\partial\overline{\mathbf{F}}}\right)\equiv-\nabla_Y\chi, \tag{31}$$

$$\chi\equiv-\frac{\partial\mathbf{w}}{\partial\overline{\mathbf{F}}}, \tag{32}$$

where a third order tensor χ is the derivative of the microscopic displacement with respect to the macroscopic deformation gradient. This is referred to as the characteristic deformation for nonlinear problems. The equation above can be substituted into Eq. (30) yielding

$$\int_{Y_0}\delta\tilde{\mathbf{Z}}:\mathbf{A}:\nabla_Y\chi dY=\int_{Y_0}\delta\tilde{\mathbf{Z}}:\mathbf{A}:\mathbf{I}dY. \tag{33}$$

By finite element discretization, the gradient of χ becomes

$$\nabla_Y \chi = [B^e][\chi^e], \tag{34}$$

in a microscopic finite element. $[\chi^e]$ is the derivative of the microscopic displacement for each component of $\overline{\mathbf{F}}$; in other words, it is the matrix given below with nine kinds of characteristic deformation.

$$[\chi^e] = \begin{bmatrix} \chi^e_{111} & \chi^e_{112} & \cdots & \chi^e_{133} \\ \chi^e_{211} & \chi^e_{212} & \cdots & \chi^e_{233} \\ \vdots & \vdots & \ddots & \vdots \\ \chi^e_{n11} & \chi^e_{n12} & \cdots & \chi^e_{n33} \end{bmatrix}, \tag{35}$$

where n is the NDOF of one finite element of the microstructure. The matrix equation becomes

$$\mathbf{K}_\chi[\chi^Q] = [\mathbf{r}_\chi], \tag{36}$$

$$\mathbf{K}_\chi = \int_{Y_0} [B^e]^T[A][B^e]dY, \tag{37}$$

$$[\mathbf{r}_\chi] = \int_{Y_0} [B^e]^T[A][I]dY, \tag{38}$$

from Eq. (33) about one microstructure. $[\chi^Q]$ denotes that the quantity is evaluated at the macroscopic quadrature point. The value of $[\chi^Q]$, which is a (NDOF of the microstructure) row $\times$ 9 column matrix, can be obtained by assembling $[\chi^e]$. $[I]$ is a ninth order identity matrix, consisting of nine column vectors $\{I_i\}(i = 1 \ldots 9)$. Thus nine solutions can be obtained for the right-hand side of Eq. (38), one for each $\{I_i\}$ corresponding to a component of the deformation gradient. $[\chi^Q]$ can then be obtained by solving each different version of the right-hand side of the above equation.

Multiplying by $[\overline{B^e}]$ and dividing by $|V|$ on both sides, Eq. (36) yields

$$\frac{1}{|V|}\mathbf{K}_\chi[\chi^Q][\overline{B^e}] = \frac{1}{|V|}[\mathbf{r}_\chi][\overline{B^e}]. \tag{39}$$

Now, by using Eq. (20)

$$\frac{1}{|V|}\mathbf{K}_\chi = \mathbf{K}^Q_{ww}, \tag{40}$$

$$\frac{1}{|V|}[\mathbf{r}_\chi][\overline{B^e}] = \mathbf{K}^Q_{wu}, \tag{41}$$

and thus,

$$\mathbf{K}^Q_{ww}[\chi^Q][\overline{B^e}] = \mathbf{K}^Q_{wu}. \tag{42}$$

The total is obtained at all macroscopic quadrature points in respect of the above equation

$$\mathbf{K}_{ww}[\chi][\overline{B}] = \mathbf{K}_{wu}, \tag{43}$$

$$[\overline{B}] \equiv \sum_i [\overline{B^e}], \tag{44}$$

$$[\chi] \equiv \sum_i [\chi^Q], \tag{45}$$

where $[\chi]$ is a matrix consisting of (quadrature points of macrostructure $\times$ NDOF of microstructure) rows $\times$ 9 columns.

The characteristic deformations are the deformation increments for unit macroscopic deformation gradients at a particular instant and these describe the material properties and strain distribution of the microstructure. Equation (29) can also be considered a linear approximation of the microscopic deformation. Therefore, the update of the microscopic deformation by

$$\Delta\mathbf{w} = -\chi : \Delta\overline{\mathbf{F}}, \tag{46}$$

corresponds to the Forward Euler method for microscopic deformation from Eq. (32).

2.4 Homogenization method using characteristic deformation mode superposition

In the mode superposition homogenization method, the microscopic displacement increment is approximately obtained by the linear combination of the previously calculated characteristic deformation ${}_0\chi$ and the scaling factor from Eq. (46) as in [10]

$$\Delta w_k \doteqdot -{}_0\chi_{kpQ}\Delta\alpha_{pQ}, \tag{47}$$

where α is the scaling factor for each mode. Inserting Eq. (47) into Eq. (22) yields the matrix

$$\begin{bmatrix} [{}_0\chi]^T & \mathbf{0} \\ \mathbf{0} & \mathbf{I} \end{bmatrix}\begin{bmatrix} \mathbf{K}_{ww} & \mathbf{K}_{wu} \\ \mathbf{K}_{uw} & \mathbf{K}_{uu} \end{bmatrix}\begin{bmatrix} [{}_0\chi] & \mathbf{0} \\ \mathbf{0} & \mathbf{I} \end{bmatrix}\begin{Bmatrix} \Delta\boldsymbol{\alpha} \\ \Delta\mathbf{u} \end{Bmatrix} = \begin{bmatrix} [{}_0\chi]^T & \mathbf{0} \\ \mathbf{0} & \mathbf{I} \end{bmatrix}\begin{Bmatrix} \mathbf{r}_w \\ \mathbf{r}_u \end{Bmatrix} \tag{48}$$

$$\begin{bmatrix} [{}_0\chi]^T\mathbf{K}_{ww}[{}_0\chi] & [{}_0\chi]^T\mathbf{K}_{wu} \\ \mathbf{K}_{uw}[{}_0\chi] & \mathbf{K}_{uu} \end{bmatrix}\begin{Bmatrix} \Delta\boldsymbol{\alpha} \\ \Delta\mathbf{u} \end{Bmatrix} = \begin{Bmatrix} [{}_0\chi]^T\mathbf{r}_w \\ \mathbf{r}_u \end{Bmatrix}, \tag{49}$$

where $[{}_0\chi]$ is the same kind of matrix as $[\chi]$. The above equation can be represented as

$$\begin{bmatrix} \mathbf{K}_{\alpha\alpha} & \mathbf{K}_{\alpha u} \\ \mathbf{K}_{u\alpha} & \mathbf{K}_{uu} \end{bmatrix}\begin{Bmatrix} \Delta\boldsymbol{\alpha} \\ \Delta\mathbf{u} \end{Bmatrix} = \begin{Bmatrix} \mathbf{r}_\alpha \\ \mathbf{r}_u \end{Bmatrix}, \tag{50}$$

where

$$\mathbf{K}_{\alpha\alpha} = \int_{\Omega} \left(\frac{1}{|V|} \int_{Y_0} [{}_0\chi^e]^T [B^e]^T [A][B^e][{}_0\chi^e] dY \right) dX, \tag{51}$$

$$\mathbf{K}_{\alpha u} = -\int_{\Omega} \left(\frac{1}{|V|} \int_{Y_0} [{}_0\chi^e]^T [B^e]^T [A] dY \right) [\overline{B^e}] dX, \tag{52}$$

$$\mathbf{K}_{u\alpha} = -\int_{\Omega} [\overline{B^e}]^T \left(\frac{1}{|V|} \int_{Y_0} [A][B^e][{}_0\chi^e] dY \right) dX, \tag{53}$$

$$\mathbf{K}_{uu} = \int_{\Omega} [\overline{B^e}]^T \left(\frac{1}{|V|} \int_{Y_0} [A] dY \right) [\overline{B^e}] dX, \tag{54}$$

$$\{\mathbf{r}_u\} = F_{ext} - \int_{\Omega} [\overline{B^e}]^T \left(\frac{1}{|V|} \int_{Y_0} [\Pi] dY \right) dX, \tag{55}$$

$$\{\mathbf{r}_\alpha\} = \int_{\Omega} \left(\frac{1}{|V|} \int_{Y_0} [{}_0\chi^e]^T [B^e]^T [\Pi] dY \right) dX. \tag{56}$$

We obtain the matrix with unknowns $\Delta\alpha$ and $\Delta\mathbf{u}$. Because the NDOF of the matrix is reduced to (NDOF of macrostructure + quadrature point of macrostructure $\times$ 9), significant computational cost is saved.

This technique is, however, an approximate means of achieving equilibrium in a range of displacements representing linear combinations of χ_0, as it is clear from Eq. (56) that χ_0 has an effect on the equilibrium. In this way, to approximate the deformation in limited deformation patterns, an approximation error is created depending on the analysis case [15].

3 Algorithm for nonlinear homogenization method

3.1 Generalized algorithm

In Eq. (22), $\{\Delta w\}$ can be statically condensed at the element quadrature point level and becomes

$$\{\Delta\mathbf{w}\} = \mathbf{K}_{ww}^{-1}(\{\mathbf{r}_w\} - \mathbf{K}_{wu}\{\Delta\mathbf{u}\}). \tag{57}$$

$\{\Delta w\}$ vanishes when the above equation is substituted in the macroscopic equilibrium equation

$$(\mathbf{K}_{uu} - \mathbf{K}_{uw}\mathbf{K}_{ww}^{-1}\mathbf{K}_{wu})\{\Delta\mathbf{u}\} = \{\mathbf{r}_u\} - \mathbf{K}_{uw}\mathbf{K}_{ww}^{-1}\{\mathbf{r}_w\}. \tag{58}$$

Now, the microscopic equilibrium hypothesized for $\overline{\mathbf{F}}$ at this time is

$$\{\mathbf{r}_w\} = 0. \tag{59}$$

By using Eqs. (43) and (57), we obtain [5]

$$\{\Delta\mathbf{w}\} = -\mathbf{K}_{ww}^{-1}\mathbf{K}_{wu}\{\Delta\mathbf{u}\} = -[\chi][\overline{\mathbf{B}}]\{\Delta\mathbf{u}\}. \tag{60}$$

By using Eqs. (43), (57), and (58) we can represent

$$(\mathbf{K}_{uu} - \mathbf{K}_{uw}[\chi][\overline{\mathbf{B}}])\{\Delta\mathbf{u}\} = \{\mathbf{r}_u\}, \tag{61}$$

where $(\mathbf{K}_{uu} - \mathbf{K}_{uw}[\chi][\overline{\mathbf{B}}])$ is called the homogenized tangent stiffness.

In differential equation form, from Eqs. (14), (17), and (31), this becomes

$$\int_{\Omega} \delta\overline{\mathbf{F}} : \left(\frac{1}{|V|} \int_{Y_0} \Big(\mathbf{A} : (\mathbf{I} - \nabla_Y \chi) \Big) dY \right) : \Delta\overline{\mathbf{F}} dX = \overline{\mathbf{F}}_{ext} - \int_{\Omega} \delta\overline{\mathbf{F}} : \left(\frac{1}{|V|} \int_{Y_0} \Pi dY \right) dX. \tag{62}$$

Microscopic equilibrium, Eq. (59),

$$r_w = \int_{Y_0} \delta\tilde{\mathbf{Z}} : \Pi dY = \mathbf{0}, \tag{63}$$

is a prerequisite of the above equation. To satisfy this nonlinear prerequisite, a Newton–Raphson iteration is needed. Thus the above equation is linearized with respect to $\mathbf{w}$ while $\overline{\mathbf{F}}$ is fixed, and then discretized by the finite element method using Eq. (19). At each quadrature point, the linearized self-equilibrated equation becomes

$$\int_{Y_0} [B^e]^T [A][B^e] dY \{\Delta\mathbf{w}^Q\} = -\int_{Y_0} [B^e]^T [\Pi] dY. \tag{64}$$

In the generalized algorithm, it is necessary to compute three different calculations in each iteration.

1. Update macroscopic tangential homogenization χ using Eq. (36).
2. Solve microscopic equilibrium problem, Eq. (63), and obtain the convergence solution $\{\mathbf{w}\}$ while $\overline{\mathbf{F}}$ is fixed.
3. Solve the linearized macroscopic equilibrium equation, Eq. (61), to obtain $\{\mathbf{u}\}$.

Processes 1 and 2 need to be solved at all quadrature points of the macrostructure and it is known that this contributes the most to the calculation load [6]. These processes require prohibitive computational cost and actual numerical simulation is difficult.

3.2 Block LU factorization algorithm

We now present an algorithm that decreases the residual of each scale simultaneously using the block LU factorization

algorithm without microscopic convergence in the macroscopic iteration as in the conventional algorithm. By block LU factorization, Eq. (22) becomes

$$\begin{bmatrix} \mathbf{K}_{ww} & \mathbf{0} \\ \mathbf{K}_{uw} & \mathbf{S} \end{bmatrix} \begin{bmatrix} \mathbf{I} & \mathbf{K}_{ww}^{-1}\mathbf{K}_{wu} \\ \mathbf{0} & \mathbf{I} \end{bmatrix} \begin{Bmatrix} \Delta\mathbf{w} \\ \Delta\mathbf{u} \end{Bmatrix} = \begin{Bmatrix} \mathbf{r}_w \\ \mathbf{r}_u \end{Bmatrix}, \tag{65}$$

where $\mathbf{S}$ is called the Schur-Complement. Referring to Eq. (43),

$$\begin{aligned} \mathbf{S} &= \mathbf{K}_{uu} - \mathbf{K}_{uw}\mathbf{K}_{ww}^{-1}\mathbf{K}_{wu} \\ &= \mathbf{K}_{uu} - \mathbf{K}_{uw}[\chi][\overline{\mathbf{B}}] \\ &= \mathbf{K}_{uu} - [\overline{\mathbf{B}}]^T[\chi]^T\mathbf{K}_{ww}[\chi][\overline{\mathbf{B}}], \end{aligned} \tag{66}$$

which corresponds to the homogenized tangent stiffness of Eq. (61). The solution process for Eq. (65) is composed of the forward substitution

$$\begin{bmatrix} \mathbf{K}_{ww} & \mathbf{0} \\ \mathbf{K}_{uw} & \mathbf{S} \end{bmatrix} \begin{Bmatrix} \Delta\tilde{\mathbf{w}} \\ \Delta\tilde{\mathbf{u}} \end{Bmatrix} = \begin{Bmatrix} \mathbf{r}_w \\ \mathbf{r}_u \end{Bmatrix}, \tag{67}$$

and the backward substitution

$$\begin{Bmatrix} \Delta\tilde{\mathbf{w}} \\ \Delta\tilde{\mathbf{u}} \end{Bmatrix} = \begin{bmatrix} \mathbf{I} & \mathbf{K}_{ww}^{-1}\mathbf{K}_{wu} \\ \mathbf{0} & \mathbf{I} \end{bmatrix} \begin{Bmatrix} \Delta\mathbf{w} \\ \Delta\mathbf{u} \end{Bmatrix}. \tag{68}$$

Then, from Eqs. (43), (67), and (68),

$$\mathbf{K}_{ww}\{\Delta\tilde{\mathbf{w}}\} = \{\mathbf{r}_w\}, \tag{69}$$

$$\mathbf{S}\{\Delta\mathbf{u}\} = \{\mathbf{r}_u\} - \mathbf{K}_{uw}\{\Delta\tilde{\mathbf{w}}\}, \tag{70}$$

$$\begin{aligned} \{\Delta\mathbf{w}\} &= \{\Delta\tilde{\mathbf{w}}\} - \mathbf{K}_{ww}^{-1}\mathbf{K}_{wu}\{\Delta\mathbf{u}\} \\ &= \{\Delta\tilde{\mathbf{w}}\} - [\chi]\Delta\overline{\mathbf{F}}, \end{aligned} \tag{71}$$

hold. The calculation process is described below.

1. Solve linearized microscopic equilibrium equation, Eq. (69), to obtain $\{\Delta\mathbf{w}\}$.
2. Solve linearized macroscopic equilibrium equation, Eq. (70), to obtain $\{\Delta\mathbf{u}\}$. Note that this equation is equivalent to Eq. (58).
3. Update $\{\Delta\mathbf{w}\}$ using Eq. (71). We have already obtained $[\chi]$ from the calculation of $\mathbf{S}$.

Three matrices, namely the micro, macro, and Schur-Complement, need to be solved at each iteration. Although the computational cost of this algorithm is expected to be lower than that of the generalized algorithm since equilibrium of the microstructure is not required at every iteration, the Schur-Complement update is still relatively expensive as described above. A similar algorithm for a differential equation using the Block-Newton method has been proposed by Yamada and Matsui [19].

3.3 Approximation of schur-complement in micro–macro coupled equation

In the block LU factorization algorithm described in the previous subsection, the linearized equations for the microstructure are solved first and then the increment for the macro-displacements is solved using the Schur-Complement that reflects the micro–macro interactions. These two steps essentially define the computational cost because the third step can be solved efficiently by reusing the characteristic deformation that has already been computed in the evaluation of the Schur-Complement in the second step. Although the macroscopic equilibrium conditions must be satisfied as well as the microscopic ones by making a convergence judgment for the residuals, the Schur-Complement is a tangent stiffness for prediction and does not influence the equilibrium directly. Hence, one of the requirements for efficient nonlinear homogenization algorithms is to approximate the Schur-Complement effectively. In this regard, we propose the two algorithms given below.

A simple method is to approximate the Schur-Complement using the previously calculated characteristic deformation ${}_0\chi$ as in

$$\begin{aligned} \mathbf{S} &= \mathbf{K}_{uu} - \mathbf{K}_{uw}[\chi][\overline{\mathbf{B}}] \\ &\doteqdot \mathbf{K}_{uu} - \mathbf{K}_{uw}[{}_0\chi][\overline{\mathbf{B}}] \\ &= \mathbf{K}_{uu} - [\overline{\mathbf{B}}]^T[\chi]^T\mathbf{K}_{ww}[{}_0\chi][\overline{\mathbf{B}}], \end{aligned} \tag{72}$$

that is,

$$[\chi]^T\mathbf{K}_{ww}[\chi] \doteqdot [\chi]^T\mathbf{K}_{ww}[{}_0\chi], \tag{73}$$

is employed from Eq. (66). Henceforth, this method is referred to as the modified block LU factorization algorithm (MBFA). The other approach is to make use of the aforementioned Mode Superposition method in the approximation of the Schur-Complement. The calculation process and an interpretation thereof are given below.

1. Solve the linearized microscopic equilibrium equation, Eq. (69), to obtain $\{\Delta\tilde{\mathbf{w}}\}$.
2. From Eq. (50), solve the mode superposition-based linearized micro–macro coupled equation

$$\begin{bmatrix} \mathbf{K}_{\alpha\alpha} & \mathbf{K}_{\alpha u} \\ \mathbf{K}_{u\alpha} & \mathbf{K}_{uu} \end{bmatrix} \begin{Bmatrix} \Delta\alpha \\ \Delta\mathbf{u} \end{Bmatrix} = \begin{Bmatrix} \mathbf{r}_\alpha \\ \mathbf{r}_u \end{Bmatrix}, \tag{74}$$

   to obtain $\{\Delta\mathbf{u}\}$. Then, $\mathbf{S}$ is approximated by the range of the mode superposition method and the update of $\mathbf{S}$ can be omitted.
3. The assumption of the mode superposition method follows from Eqs. (46), (47), and (71), and $\{\Delta\mathbf{w}\}$ is updated using

$$\{\Delta \mathbf{w}\} = \{\Delta \tilde{\mathbf{w}}\} - [_0\chi]\{\Delta\alpha\}. \tag{75}$$

The meaning of the algorithm is now given. Block LU factorization is applied to Eq. (74) yielding

$$\mathbf{K}_{\alpha\alpha}\{\Delta\tilde{\alpha}\} = \{\mathbf{r}_\alpha\}, \tag{76}$$

$$(\mathbf{K}_{uu} - \mathbf{K}_{u\alpha}\mathbf{K}_{\alpha\alpha}^{-1}\mathbf{K}_{\alpha u})\{\Delta\mathbf{u}\} = \{\mathbf{r}_u\} - \mathbf{K}_{u\alpha}\{\Delta\tilde{\alpha}\}, \tag{77}$$

$$\{\Delta\alpha\} = \{\Delta\tilde{\alpha}\} - \mathbf{K}_{\alpha\alpha}^{-1}\mathbf{K}_{\alpha u}\{\Delta\mathbf{u}\}. \tag{78}$$

In Eq. (77), the macroscopic displacement is updated using

$$(\mathbf{K}_{uu} - \mathbf{K}_{u\alpha}\mathbf{K}_{\alpha\alpha}^{-1}\mathbf{K}_{\alpha u}), \tag{79}$$

which can be considered an approximation of the homogenized tangent stiffness. Then, using Eqs. (43) and (66), the Schur-Complement becomes

$$\begin{aligned}
\mathbf{S} &= \mathbf{K}_{uu} - \mathbf{K}_{uw}[\chi][\overline{\mathbf{B}}] \\
&= \mathbf{K}_{uu} - \mathbf{K}_{uw}[\chi]([\chi]^T\mathbf{K}_{ww}[\chi])^{-1}([\chi]^T\mathbf{K}_{ww}[\chi])[\overline{\mathbf{B}}] \\
&= \mathbf{K}_{uu} - \mathbf{K}_{uw}[\chi]([\chi]^T\mathbf{K}_{ww}[\chi])^{-1}[\chi]^T\mathbf{K}_{wu} \\
&\doteqdot \mathbf{K}_{uu} - \mathbf{K}_{uw}[_0\chi]([_0\chi]^T\mathbf{K}_{ww}[_0\chi])^{-1}[_0\chi]^T\mathbf{K}_{wu} \\
&= \mathbf{K}_{uu} - [\overline{\mathbf{B}}]^T[\chi]^T\mathbf{K}_{ww}[_0\chi] \\
&\quad \times([_0\chi]^T\mathbf{K}_{ww}[_0\chi])^{-1}[_0\chi]^T\mathbf{K}_{ww}[\chi][\overline{\mathbf{B}}] \\
&= \mathbf{K}_{uu} - \mathbf{K}_{u\alpha}\mathbf{K}_{\alpha\alpha}^{-1}\mathbf{K}_{\alpha u},
\end{aligned} \tag{80}$$

that is,

$$\begin{aligned}
&[\chi]^T\mathbf{K}_{ww}[\chi] \doteqdot [\chi]^T\mathbf{K}_{ww}[_0\chi] \\
&\quad \times([_0\chi]^T\mathbf{K}_{ww}[_0\chi])^{-1}[_0\chi]^T\mathbf{K}_{ww}[\chi],
\end{aligned} \tag{81}$$

is employed. In the mode superposition method, since the homogenized tangent stiffness corresponds to the exact value with the mode updated at every Newton–Raphson iteration as described above, this method can give an approximate mean of the homogenized tangent stiffness by decreasing the number of times that the mode is updated. This method is referred to as the mode superposition algorithm (MSA).

4 Numerical examples

4.1 Comparison of computational costs and convergence properties

With respect to computational cost and convergence, which are of interest to us, we now compare the four methods introduced in the previous section, namely, the generalized algorithm (GA), block LU factorization algorithm (BFA), modified block LU factorization algorithm (MBFA) and the algorithm using mode superposition (MSA). Detailed algorithms for the parallel computation of each of the methods are given in Fig. 2. The GA calculates the microscopic equilibrium at each quadrature point in every iteration. In contrast to the GA, the BFA, MBFA, and MSA decrease the residual

1. Set calculation condition
2. Perform in a unit cell at each quadrature point by paraell computation
   Solve microscopic equilibrium problem : $\{\mathbf{r}_w\} = 0$
   Update the microscopic deformation : $\{\mathbf{w}\}$
   Solve for update χ : $\mathbf{K}_\chi[\chi^Q] = [\mathbf{r}_\chi]$
   Compute : $\mathbf{K}_{uu} - \mathbf{K}_{uw}\mathbf{K}_{ww}^{-1}\mathbf{K}_{wu}, \{\mathbf{r}_u\}$
3. Communication using MPIallreduce
   Assemble : $\mathbf{K}_{uu} - \mathbf{K}_{uw}\mathbf{K}_{ww}^{-1}\mathbf{K}_{wu}, \{\mathbf{r}_u\}$
4. Solve
   $$(\mathbf{K}_{uu} - \mathbf{K}_{uw}[\chi][\overline{\mathbf{B}}])\{\Delta\mathbf{u}\} = \{\mathbf{r}_u\}$$
5. Update the vatiables
   $$\{\mathbf{u}\} = \{\mathbf{u}\} + \{\Delta\mathbf{u}\}$$
6. if $|\{\mathbf{r}_u\}| < Tol$, then
   Next step GOTO 1
   else
   Next iteration GOTO 2

(a)

1. Set calculation condition
2. Perform in a unit cell at each quadrature point by paraell computation
   Compute : $\mathbf{K}_{ww}, \{\mathbf{r}_w\}$
   Solve : $\mathbf{K}_{ww}\{\Delta\tilde{\mathbf{w}}\} = \{\mathbf{r}_w\}$
   Update the microscopic deformation: $\{\mathbf{w}\} = \{\mathbf{w}\} + \{\Delta\tilde{\mathbf{w}}\}$
   In the BFA, everytime solve for update χ : $\mathbf{K}_\chi[\chi^Q] = [\mathbf{r}_\chi]$
   (In the MBFA, sometime solve for update χ_0 : $\mathbf{K}_\chi[\chi^Q] = [\mathbf{r}_\chi]$)
   Compute : $\mathbf{S}, \{\mathbf{r}_u\} - \mathbf{K}_{uw}\{\Delta\tilde{\mathbf{w}}\}$
3. Communication using MPIallreduce
   Assemble : $\mathbf{S}, \{\mathbf{r}_u\} - \mathbf{K}_{uw}\{\Delta\tilde{\mathbf{w}}\}$
4. Solve
   $$\mathbf{S}\{\Delta\mathbf{u}\} = \{\mathbf{r}_u\} - \mathbf{K}_{uw}\{\Delta\tilde{\mathbf{w}}\}$$
5. Update the vatiables
   $\{\mathbf{u}\} = \{\mathbf{u}\} + \{\Delta\mathbf{u}\}$
   In the BFA, $\{\mathbf{w}\} = \{\tilde{\mathbf{w}}\} - [\chi]\Delta\overline{\mathbf{F}}$
   In the MBFA, $\{\mathbf{w}\} = \{\tilde{\mathbf{w}}\} - [\chi_0]\Delta\overline{\mathbf{F}}$
6. if $|\{\mathbf{r}_w\}| < Tol, |\{\mathbf{r}_u\}| < Tol$, then
   Next step GOTO 1
   else
   Next iteration GOTO 2

(b)

1. Set calculation condition
2. Perform in a unit cell at each quadrature point by paraell computation
   Compute : $\mathbf{K}_{ww}, \{\mathbf{r}_w\}$
   Solve : $\mathbf{K}_{ww}\{\Delta\tilde{\mathbf{w}}\} = \{\mathbf{r}_w\}$
   Update the microscopic deformation: $\{\mathbf{w}\} = \{\mathbf{w}\} + \{\Delta\tilde{\mathbf{w}}\}$
   (Sometime solve for update χ_0 : $\mathbf{K}_\chi[\chi^Q] = [\mathbf{r}_\chi]$)
   Compute : $\mathbf{K}_{uu}, \mathbf{K}_{u\alpha}, \mathbf{K}_{\alpha u}, \mathbf{K}_{\alpha\alpha}, \{\mathbf{r}_\alpha\}, \{\mathbf{r}_u\}$
3. Communication using MPIallreduce
   Assemble : $\mathbf{K}_{uu}, \mathbf{K}_{u\alpha}, \mathbf{K}_{\alpha u}, \mathbf{K}_{\alpha\alpha}, \{\mathbf{r}_\alpha\}, \{\mathbf{r}_u\}$
4. Solve
   $$\begin{bmatrix}\mathbf{K}_{\alpha\alpha} & \mathbf{K}_{\alpha u}\\ \mathbf{K}_{u\alpha} & \mathbf{K}_{uu}\end{bmatrix}\begin{Bmatrix}\Delta\alpha\\ \Delta\mathbf{u}\end{Bmatrix} = \begin{Bmatrix}\mathbf{r}_\alpha\\ \mathbf{r}_u\end{Bmatrix}$$
5. Update the vatiables
   $$\{\mathbf{u}\} = \{\mathbf{u}\} + \{\Delta\mathbf{u}\}$$
   $$\{\alpha\} = \{\alpha\} + \{\Delta\alpha\}$$
   $$\{\mathbf{w}\} = \{\tilde{\mathbf{w}}\} - [_0\chi]\{\Delta\alpha\}$$
6. if $|\{\mathbf{r}_w\}| < Tol, |\{\mathbf{r}_u\}| < Tol$, then
   Next step GOTO 1
   else
   Next iteration GOTO 2

(c)

Fig. 2 Algorithms for parallel computation using the message passing interface (MPI). **a** Algorithms for GA. **b** Algorithms for BFA and MBFA. **c** Algorithms for MSA

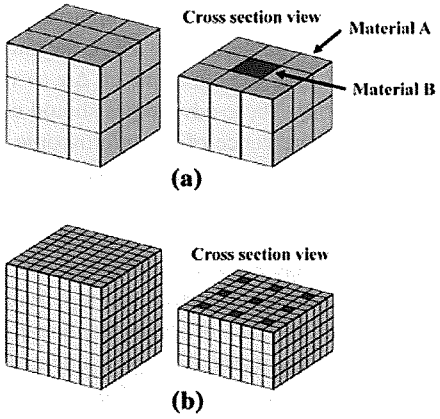

Fig. 3 FE models used in the calculation time evaluation. **a** 64 nodes, 27 elements (minimum size). **b** 1000 nodes, 729 elements

Table 1 Material constants for the models used in the calculation time evaluation

	E[kPa]	ν
Material A in Fig. 3	0.1	0.3
Material B in Fig. 3	10.0	0.3

of both scales simultaneously. Moreover, in the MBFA and MSA the straightforward update of S is avoided. We performed a 20% tensile test using the mesh of the block shown in Fig. 3 as the microstructure, and a single 8-node element as the macrostructure. The minimum size of the mesh is constructed from 27 (3 × 3 × 3) elements as shown in Fig. 3a, with the stiffness of the center element different from the rest.

The NDOF is adjusted by adding the same number of minimum units in each direction (e.g. Fig. 3b). The St. Venant hyperelastic material is used for the constitutive equations

$$W = \frac{1}{2}\lambda(tr\mathbf{E})^2 + \mu\mathbf{E} : \mathbf{E}, \tag{82}$$

$$\mathbf{S} = \frac{\partial W}{\partial \mathbf{E}} = (\lambda\mathbf{I} \otimes \mathbf{I} + 2\mu\mathbf{I}) : \mathbf{E} = \mathbf{C} : \mathbf{E}, \tag{83}$$

$$l_{ijkl} = \delta_{ik}\delta_{jl}, \tag{84}$$

$$\lambda = \frac{E\nu}{(1+\nu)(1-2\nu)}, \quad \mu = G = \frac{E}{2(1+\nu)}, \tag{85}$$

where $\mathbf{I}$ is a second order identity tensor, λ and μ are Lame constants, and E and ν are, respectively, Young's modulus and Poisson's ratio. $\mathbf{C}$ is a fourth order constant elasticity tensor and the relationship between S and E is linear. The material constants are given in Table 1. If the material constants are assumed to be uniform in the microstructure, the solutions obtained by these methods agree completely with the theoretical solution in the case of infinitesimal deformation. We have thus confirmed the correctness of the formulations

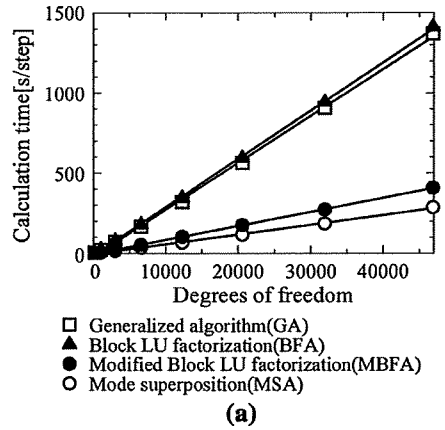

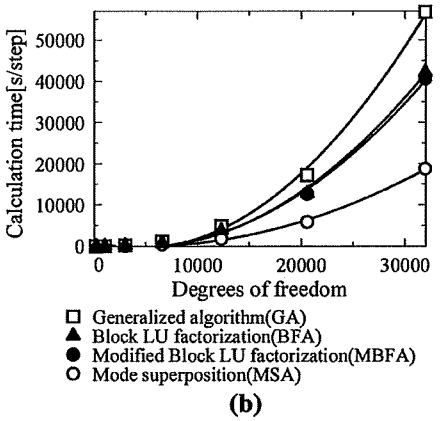

Fig. 4 Comparison of calculation time. **a** Iterative solver. **b** Direct solver

and computer programs. The relationship between calculation time and NDOF of the microstructure for each algorithm is depicted in Fig. 4 for cases where an iterative solver (ILU preconditioned GMRES method) or direct solver (skyline method) are used. The breakdown of calculation time and number of iterations in each process, where the NDOF of the microstructure is 31,944, are given in Table 2. Convergence is judged to occur when the root sum square reaches 1×10^{-10} times the initial value. As shown in Fig. 4, the calculation time of the BFA using an iterative solver slightly exceeds that of the GA. In the BFA, equilibrium of the microstructure is not required within an iteration for the sake of computational efficiency, but this may result in more iterations compared with the GA. Table 2 illustrates this, in that the BFA requires 5 iterations whereas the GA requires 4. We need to calculate the characteristic deformation to update the Schur-Complement; this means that the nine different right-hand sides of Eq. (33) must be solved in the case of the iterative solver. Consequently, the increased number of iterations results in a deterioration in the performance of the BFA. If a direct solver is used instead, the result of the LU decomposition

Table 2 Calculation time and number of iterations in each process

	Calculation of χ (s)	Calculation of equilibrium in the microscopic model (s)	Total (s)	No. of iterations
a. Iterative solver				
GA	670	211	906	4
BFA	805	107	942	5
MBFA	17	195	273	11
MSA	21	113	186	5
b. Direct solver				
GA	19,816	36,949	56,791	4
BFA	23,689	18,492	42,212	5
MBFA	451	40,050	40,557	11
MSA	457	18,237	18,746	5

of the stiffness matrix can be reused in the computation of the characteristic deformation, and as a result, the computational cost of the BFA is 20% less than that of the GA, despite the BFA using one more iteration than the GA. On the other hand, the MBFA is much faster than both the BFA and the GA when an iterative solver is used, although in the case of a direct solver there is almost no difference between the MBFA and BFA. This is because the calculation cost of the mode update in the BFA is similar to that of the increased iterations in the MBFA. However, convergence in the MBFA is slow as shown in Fig. 5 and it is anticipated that for strong nonlinear problems, convergence may not be achieved at all. Here, the characteristic deformation was approximated by that obtained at the beginning of the analysis. Convergence can be improved by incorporating more frequent updates, at the expense of CPU time. Compared with these methods, the MSA always exhibits excellent speed and convergence. The advantage of the MSA is twofold. First, the approximation of the Schur-Complement is more accurate than in the MBFA, i.e., Eq. (80) gives a superior approximation than Eq. (72). Second, in an iteration of the MSA, the microscopic equation is solved in Eq. (75) in terms of $\Delta\alpha$ as well as in Eq. (74) with Eq. (69). These advantages should contribute to an accelerated convergence of the microscopic equation as well as the macroscopic equation. Although the St. Venant hyperelastic material assumed here has relatively weak nonlinearity, the number of iterations does not increase up to a large deformation range, even with the initial characteristic deformation being used for ${}_0\chi$. However, a periodic update of ${}_0\chi$ is required in the case of strong nonlinear material, such as an elasto-plastic material. If ${}_0\chi$ is updated at every iteration, the homogenized tangent stiffness corresponds to the exact value as described in Eq. (80).

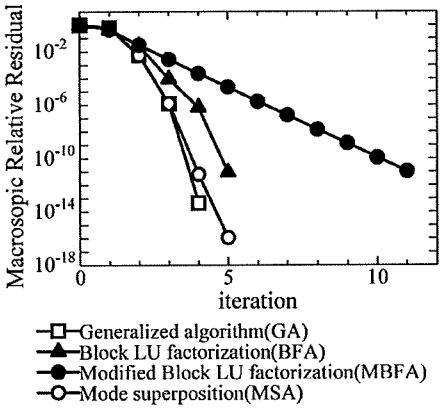

Fig. 5 Comparison of convergence property

4.2 Application to ventricle–cardiomyocyte analysis with parallel computation

As seen in Table 2, most of the calculation cost relates to the microscopic equilibrium (Eq. (69)) when the MBFA or MSA is used. In addition, as the NDOF of the microscopic model becomes larger, the computational cost for the macroscopic model becomes more negligible. It is therefore crucial to decrease the time for microscopic calculation in real problems. Since Eq. (69) holds independently at each macroscopic quadrature point, parallel computation is effective in the homogenization method. In other words, microscopic models can be distributed equally to the available cores, and this directly accelerates the microscopic calculation according to the number of cores. Moreover, since the memory is shared by fewer microscopic models in the parallel computation, a greater NDOF of the microstructure can be handled.

Figures 6 and 7 show a simplified human cardiomyocyte–ventricle model, to which we have applied the MSA. As shown on the left and in the center of Fig. 7 a simplified cardiomyocyte model is constructed with extracellular and intracellular matrices and gap junctions. The total NDOF is 20385. If the models are arrayed periodically in the three directions as depicted on the right of the figure, a fairly accurate imitation of a microgram of real tissue is obtained. The

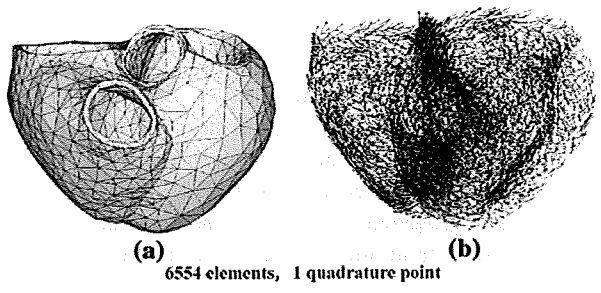

Fig. 6 FE meshes of ventricles as macroscopic model. **a** FE mesh. **b** Fiber orientation

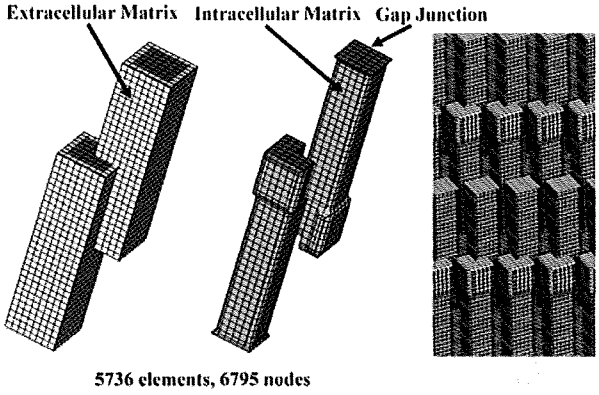

Fig. 7 FE meshes of cardiomyocytes as microscopic model

Table 3 Material constants for the cell model

	C_1	C_2	κ
Gap Junction	1×10^5	1×10^5	2×10^5
Intracellular Matrix	1×10^4	1×10^4	2×10^4
Extracellular Matrix	1×10^3	1×10^3	2×10^3

Mooney–Rivlin material using reduced invariants is adopted for the constitutive equation, with the material constants listed in Table 3.

$$W = C_1(\tilde{I}_c - 3) + C_2(\tilde{II}_c - 3) + \frac{\kappa}{2}U^2 \tag{86}$$

$$\tilde{I}_c = \frac{I_c}{III_c^{1/3}}, \quad \tilde{II}_c = \frac{II_c}{III_c^{2/3}} \tag{87}$$

$$U = J - 1, \tag{88}$$

where U is the volumetric strain energy function and κ is the bulk modulus. The ventricle model is constructed based on CT imaging, with fiber directions distributed from -90 to 60 degrees, relative to the plane perpendicular to the long axis of the ventricle. The fiber direction denotes the long axis (z-axis) of the cardiomyocyte model, and therefore, proper rotation is taken into consideration for each micromodel. In this model, the intracellular matrix is defined as a function of a parameter that represents the excitation of the myocyte, and this parameter is varied at every time step to represent the transient contraction force. The homogenization method is applied to 6,554 elements covering the greater region of the ventricle, whereas the conventional Mooney–Rivlin hyperelastic constitutive law is assumed for the limited regions at the base and apex. To reduce the computational cost, a single myocyte (micromodel) is assigned to each finite element of the ventricle, i.e., 6,554 cardiomyocyte models are embedded in the ventricle model. The total NDOF, including those of the ventricles, amounts to 133,609,263.

The computer used was an IBM Blade Center consisting of 336 Power6 (4.0 GHz) processors. Considering the size of the problem, convergence was deemed to occur when the root sum square of the macro and micro residuals was 1×10^{-5} times less than the initial value. Figure 8 shows the maximum, the minimum and the mean Green–Lagrange strains throughout the ventricle model, and the number of iterations of the MSA at each time step. The strains are measured in the fiber direction. Although the maximum and the minimum strains reach $\pm 20\%$, an excellent convergence property was observed. Figure 9 shows the resulting scalability, by depicting the speed up rate relative to a hundred-core computation. As shown in this figure, satisfactory parallel performance was obtained by the proposed algorithm. The deformations of the ventricle and a representative myocyte in the diastole and the systole are exemplified in Fig. 10. The CPU time for the completion of a cardiac cycle was about 24 h when using 300 cores. The proposed method thus allows us to deal with large-scale problems.

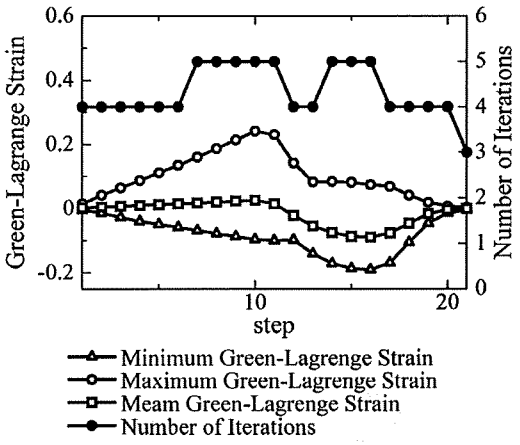

Fig. 8 Green–Lagrenge strains and nunber of iterations at each step

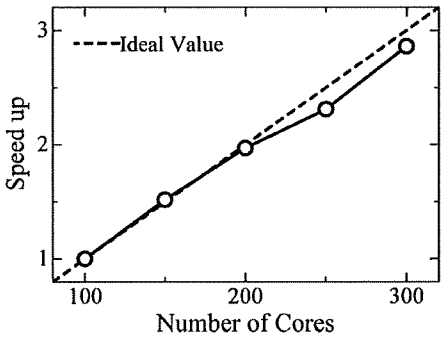

Fig. 9 Speed up in parallel computation

5 Conclusion

To reduce the computational cost of the nonlinear homogenization method, the theoretical framework was reassessed

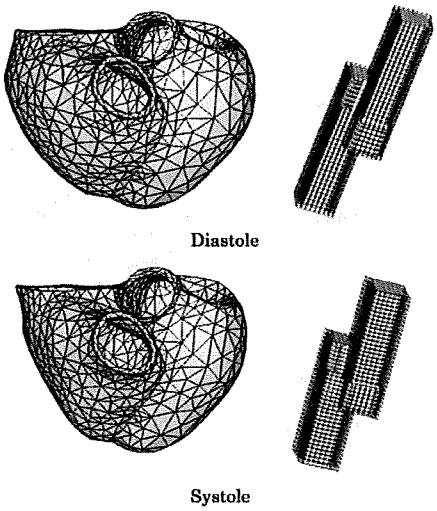

Fig. 10 Deformations of macro and microstructures in diastole and systole

from the perspective of block LU factorization of the micro–macro coupled equation. Based on the relation between the characteristic deformation and the Schur-Complement as the homogenized tangent stiffness, a couple of approximation methods were introduced, namely, a simple scheme to reuse the old characteristic deformation (MBFA) and a sophisticated method based on the mode-superposition method (MSA) developed by our group. It is noted that accuracy is preserved in these approximation methods by incorporating the equilibrium conditions in both scales. Then, using a simplified FE model, the conventional algorithm (GA), a relative algorithm originating from the block LU factorization (BFA), the MBFA, and the MSA were compared and discussed. Of these methods, the MSA was found to be the best. Then, using the MSA, a large-scale human ventricle–cardiomyocyte simulation was performed on an IBM Blade Center consisting of 336 Power6 processors, and good parallel performance was demonstrated. We plan to use the proposed homogenization algorithm in a whole-heart simulation on a massively parallel computer in the near future.

Acknowledgments Our current research on homogenization method stems from Reference [10] coauthored by Hirohisa Noguchi. We again recognize his enthusiasm and contribution in a broad range of computational mechanics. This work was supported by Core Research for Evolutional Science and Technology, Japan Science and Technology Agency.

References

1. Terada K, Hori M, Kyoya T, Kikuchi N (2000) Simulation of the multi-scale convergence in computational homogenization approaches. Int J Solids Struct 37:2285–2311
2. Hollister SJ, Kikuchi N (1992) Comparison of homogenization and standard mechanics analyses for periodic porous composites. Comput Mech 10:73–95
3. Breuls RGM, Sengers BG, Oomens CWJ, Bouten CVC, Baaijens FPT (2002) Predicting local cell deformations in engineered tissue constructs: a multilevel finite element approach. ASME J Biomech Eng 124:198–207
4. Krassowska W, Pilkington TC, Ideker RE (1990) Potential distribution in three-dimensional periodic myocardium: Part I. Solution with two-scale asymptotic analysis. IEEE Trans Biomed Eng 37:252–266
5. Terada K, Kikuchi N (2001) A class of general algorithms for multi-scale analyses of heterogeneous media. Comput Methods Appl Mech Eng 190:5427–5464
6. Matsui K, Terada K, Yuge K (2004) Two-scale finite element analysis of heterogeneous solids with periodic microstructures. Comput Struct 82:593–606
7. Takano N, Ohnishi Y, Zako M, Nishiyabu K (2001) Microstructure-based deep-drawing simulation of knitted fabric reinforced thermoplastics by homogenization theory. Int J Solids Struct 38:6333–6356
8. Rohan E (2003) Sensitivity strategies in modelling heterogeneous media undergoing finite deformation. Math Comput Simul 61:261–270
9. Moulinec H, Suquet P (1998) A numerical method for computing the overall response of nonlinear composites with complex microstructure. Comput Methods Appl Mech Eng 157:69–94
10. Yamamoto M, Hisada T, Noguchi H (2001) Homogenization method for large deformation problem by using characteristic deformation mode superposition. Trans Jpn Soc Mech Eng 67:1877–1884 (in Japanese)
11. Yamamoto M, Hisada T (2002) A homogenization method for nearly incompressible materials by using characteristic deformation mode superposition. Trans Jpn Soc Mech Eng A 45:596–602
12. Okada J, Hisada T (2006) Homogenization method for mixed finite element analysis of incompressible hyper-elastic materials. In: JSCES e06: Proceedings of the 11th computational engineering conference, Osaka, Japan, pp 79–82 (in Japanese)
13. Okada J, Hisada T (2006) Homogenization method for mixed finite element analysis of incompressible viscoelastic materials. In: Proceedings of the 19th JSME computational mechanics conference, Nagoya, Japan, pp 45–46 (in Japanese)
14. Okada J, Hisada T (2009) Study on compressibility control of hyperelastic material for homogenization method using mixed finite element analysis. J Comput Sci Technol 3(1):89–100
15. Okada J, Washio T, Hisada T (2009) Nonlinear homogenization algorithms with low computational cost. J Comput Sci Technol 3(1):101–114
16. Miehe C, Schroder J, Schotte J (1999) Computational homogenization analysis in finite plasticity. Simulation of texture development in polycrystalline materials. Comput Methods Appl Mech Eng 171:387–418
17. Allaire G (1992) Homogenization and two-scale convergence. SIAM J Math Anal 23:1482–1518
18. Terada K, Kikuchi N (2003) Introduction to the method of homogenization. Maruzen (in Japanese)
19. Yamada T, Matsui K (2007) Numerical procedure for nonlinear multiscale problems based on block Newton method. Proc Conf Comput Eng Sci 12:309–312 (in Japanese)

Artificial Organs

Artificial Organs
33(9):767–773, Wiley Periodicals, Inc.

Thoughts and Progress

Baroreflex Sensitivity of an Arterial Wall During Rotary Blood Pump Assistance

*Tomoyuki Yambe, *Kou Imachi, *Yasuyuki Shiraishi, †Tasuku Yamaguchi, ‡Mune-ichi Shibata, §Takeshi Kameyama, **Makoto Yoshizawa, and **Norihiro Sugita

*Department of Medical Engineering and Cardiology, Institute of Development, Aging and Cancer, Tohoku University, †Tohoku Kouseinenkin Hospital, ‡Miyagi Prefectural Cardio-respiratory Center, §Miyagi Shakaihoken Hospital, **Information Synergy Center, Tohoku University, Tohoku, Japan

Abstract: It is well known that the baroreflex system is one of the most important indicators of the pathophysiology in hypertensive patients. We can check the sensitivity of the baroreflex by observing heart rate (HR) responses; however, there is no simple diagnostic method to measure the arterial behavior in the baroreflex system. Presently, we report the development of a method and associated hardware that enables the diagnosis of baroreflex sensitivity by measuring the responses of both the heart and the artery. In this system, the measurements are obtained by monitoring an electrocardiogram and a pulse wave recorded from the radial artery or fingertip. The arterial responses were measured in terms of the pulse wave velocity (PWV) calculated from the pulse wave transmission time (PTT) from the heart to the artery. In this system, the HR change corresponding to the blood pressure change in time series sequence was observed. Slope of the changes in blood pressure and HR indicated the sensitivity of the baroreflex system of the heart. This system could also measure the sensitivity of the baroreflex system of an artery. Changes in the PWV in response to the blood pressure changes were observed. Significant correlation was observed in the time sequence between blood pressure change and PWV change after calculating the delay time by cross-correlation. The slope of these parameter changes was easily obtained and it demonstrated the sensitivity of the baroreflex system of an artery. We evaluated this method in animal experiments using rotary blood pump (RBP) with undulation pump ventricular assist device, and PTT elongation was observed in response to increased blood pressure with RBP assistance. Furthermore, when tested clinically, decreased sensitivity of the baroreflex system in hypertensive patients was observed. This system may be useful when we consider the ideal treatment and follow-up of patients with hypertension. **Key Words:** Baroreflex sensitivity—Arterial baroreflex—Baroreceptor—Pulse wave transmission time—Pulse wave velocity—Rotary blood pump.

doi:10.1111/j.1525-1594.2009.00864.x

Received December 2008; revised March 2009.

Address correspondence and reprint requests to Dr. Tomoyuki Yambe, 4-1 Seiryo-machi, Aoba-ku, Sendai 980-8575, Japan. E-mail; yambe@idac.tohoku.ac.jp

Presented in part at the 16th Congress of the International Society for Rotary Blood Pumps held Oct. 2–4, 2008 in Houston, TX, USA.

The baroreflex system is a key indicator of hypertensive pathophysiology (1–4). When blood pressure (BP) increases, heart rate (HR) decreases, and there is peripheral arterial dilation (1–6). By decreasing the cardiac output and peripheral arterial resistance, BP returns to normal. Hypertension is a concern in the young as well as the elderly (4–6). Baroreflex sensitivity is reduced in younger hypertensive patients (4–6). However, currently there is no simple and sensitive diagnostic method to measure the arterial behavior in the baroreflex system.

Both responses of the HR and vasomotor components are important when we consider the precise quantitative diagnosis of the autonomic nervous system mediating the baroreflex system in the human body. However no one has reported the methodology to evaluate the vasomotor components in the baroreflex system. No report describing the baroreflex sensitivity in vasomotor components can be cited currently according to PubMed. So, we cannot evaluate the importance of the HR in baroreflex sensitivity, because we cannot evaluate the vasomotor components.

Several investigators suggested the regional differentiation in autonomic responses in various human body areas. So, we cannot evaluate total response of the baroreflex system by only observing the HR. It may be a disadvantage if we cannot evaluate the precise quantification of the baroreflex system. Precise evaluation may be clearly desirable when we consider the ideal treatment and follow-up of patients with hypertension.

This study describes the development and clinical application of a new novel baroreflex diagnostic machine and offers a preliminary consideration of its clinical applicability in patients with rotary blood pump assistance.

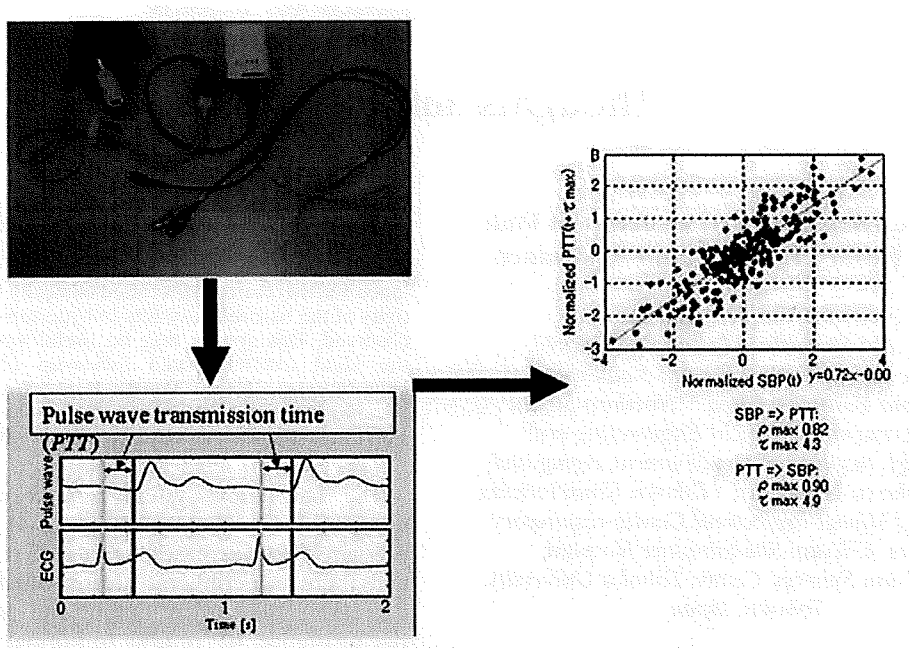

FIG. 1. Schematic diagram to explain the PWV and PTT. A photograph of the measurement equipment is shown on the upper left side. By the use of the ECG and finger tip artery waveform, we can calculate the PTT from R wave in ECG and rising point of radial arterial pressure waveform. An example of the correlation between the normalized systolic BP and normalized PTT in a patient is shown on the right. Significant correlation was observed, and the slope, suggesting the baroreflex sensitivity of an arterial tree, was calculated from the regression line from least square method.

DIAGNOSIS OF ARTERIAL BAROREFLEX SENSITIVITY

Every medical student studies the baroreflex system as a typical example of homeostasis (1–6). When BP increases, baroreceptors in the carotid arteries and aortic arch sense this. The carotid sinus baroreceptors are innervated by the glossopharyngeal nerve, the aortic arch baroreceptors are innervated by the vagus nerve. With information transmitting to the central nervous system, the HR lowers and arteries dilate by coupling sympathetic inhibition and parasympathetic activation.

In the conventional method, the baroreflex sensitivity was evaluated by measuring the HR response to the BP changes. Although HR response in the baroreflex system can be monitored, no method currently exists to evaluate arterial baroreflex function, possibly because of the difficulty in evaluating vascular tone during wakefulness.

Recently, new methodologies like brachial-ankle pulse wave velocity (baPWV) have been developed to evaluate human arterial stiffness (7–10). These methodologies non-invasively evaluate arterial wall stiffness using the pulse waveform of the brachial and ankle arteries. These methodologies are based on the premise that PWV is correlated with arterial wall stiffness. Thus, PWV increases when the arterial wall becomes harder and decreases when the arterial wall softens. PWV can be calculated from the pulse wave transmission time (PTT) and distance (Fig. 1). Thus, measurements of PTT and BP permit an evaluation of arterial baroreflex response. Time was calculated from the R wave in the electrocardiogram (ECG) and upsloping point of pressure waveform.

PTT and PWV were easily measured by monitoring ECG and pulse wave. Figure 1 shows the equipment used for the measurement. The newly developed system used only an ECG and a pulse wave recorded from the radial artery. These time series were inputted into a personal computer, and analyzed quantitatively using custom-developed software. HR was calculated from the reciprocal of the inter-R-wave interval of the ECG signal. PTT was defined as the time interval from the peak of the R wave to the point at which the pulse wave signal began to increase. HR and PTT were interpolated by cubic spine functions to continuous-time functions, and were resampled every 0.5 s.

The right side of Fig. 1 displays an example of the correlation between the systolic BP and

PTT. PTT was plotted after 6.0 s. Significant correlation was evident in the time sequence between BP change and PTT change after calculating the delay time by cross-correlation. The slope of these parameter changes was easily obtained, and it demonstrated the sensitivity of the baroreflex system of an artery.

The utility of this system for the quantitative diagnosis of the baroreflex sensitivity of an artery was recognized by the patent application.

UNDULATION PUMP VENTRICULAR ASSIST DEVICE (UPVAD) AND PTT CHANGE IN RESPONSE TO BP CHANGE

On the basis of this method, rotary blood pump with undulation pump was used in experiments to evaluate the arterial response to the rotary blood pump assistance (11,12). A healthy adult goat with UPVAD rotary blood pump was used in this experiment and results are shown in Fig. 2. If we added the rotary blood pump assistance, BP was increased and the PTT was increased in response. However, the results were influenced by the HR, of course. So, we added the pacemaker on this experiment and the results are shown in Fig. 2. During pacing, PTT was also increased in response to BP change with RBP assistance.

So, this information is also useful when we consider the hemodynamics with RBP assistance.

CONCLUSIONS

The arterial responses were measured in terms of the PWV calculated from the PTT from the heart to an artery (13,14). In this system, the HR change corresponding to the BP change in time series sequence was observed. Delay time was measured by the cross-correlation function. Slope of the changes in BP and HR indicates the sensitivity of the baroreflex system of heart. Furthermore, this system could also measure the sensitivity of the baroreflex system of an artery.

Clinical research of our study has begun after ethical committee allowance. So far, the results have shown that our system can successfully detect decreased sensitivity of the baroreflex system in hypertensive patients. We are now analyzing the various data of the patients with hypertension by gathering data from related hospitals.

Further examination will be needed using more cases. This new method may be useful to follow up patients with hypertension.

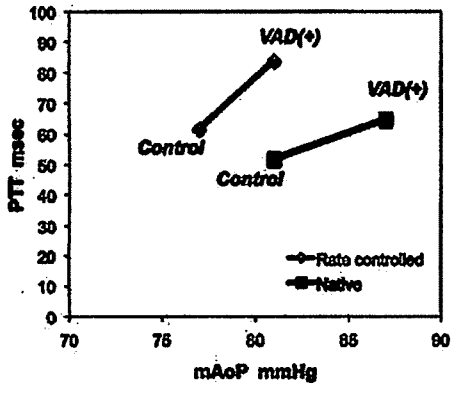

FIG. 2. An example of a PTT response to the rotary blood pump assistance with and without pacemaker. If we added the rotary blood pump assistance with UPVAD, BP was increased and the PTT was increased in response. However, the results were influenced by the HR, of course. So, we added the pacemaker on this experiment. During pacing, PTT was also increased in response to BP change with RBP assistance.

Acknowledgements: This work was partly supported by the support of Tohoku University Global COE Program "Global Nano-Biomedical Engineering Education and Research Network Centre" and research grants from Mitsui Sumitomo Insurance Welfare Foundation, Nakatani Electronic Measuring Technology Association of Japan, Japan Epilepsy Research Foundation, and the Naito Foundation.

REFERENCES

1. Grassi G, Dell'Oro R, Quarti-Trevano F, et al. Neuroadrenergic and reflex abnormalities in patients with metabolic syndrome. *Diabetologia* 2005;48:1359–65.
2. Chen HI. Mechanism of alteration in baroreflex cardiovascular responses due to volume loading. *Jpn J Physiol* 1978;28: 749–56.
3. Goldstein DS, Harris AH, Brady JV. Baroreflex sensitivity during operant blood pressure conditioning. *Biofeedback Self Regul* 1977;2:127–38.
4. Krontoradova K, Honzikova N, Fiser B, et al. Overweight and decreased baroreflex sensitivity as independent risk factors for hypertension in children, adolescents, and young adults. *Physiol Res* 2007;May 30 (Epub ahead of print).
5. Fu Q, Townsend NE, Shiller SM, et al. Intermittent hypobaric hypoxia exposure does not cause sustained alterations in autonomic control of blood pressure in young athletes. *Am J Physiol Regul Integr Comp Physiol* 2007;292:R1977–84. Epub 2007 Jan 4.
6. Honzikova N, Novakova Z, Zavodna E, et al. Baroreflex sensitivity in children, adolescents, and young adults with essential and white-coat hypertension. *Klin Padiatr* 2006;218:237–42.
7. Yambe T, Kovalev YA, Milyagina IA, et al. Japanese-Russian collaborative study on aging and atherosclerosis. *Biomed Pharmacother* 2004;58:S91–4.
8. Yamashina A, Tomiyama H, Arai T, et al. Nomogram of the relation of brachial-ankle pulse wave velocity with blood pressure. *Hypertens Res* 2003;26:801–6.
9. Yambe T, Meng X, Hou X, et al. Cardio-ankle vascular index (CAVI) for the monitoring of the atherosclerosis after heart transplantation. *Biomed Pharmacother* 2005;59:S177–9.

10. Yambe T, Yoshizawa M, Saijo Y, et al. Brachio-ankle pulse wave velocity and cardio-ankle vascular index (CAVI). *Biomed Pharmacother* 2004;58:S95–8.
11. Yambe T, Abe Y, Imachi K, et al. Development of an implantable undulation type ventricular assist device for control of organ circulation. *Artif Organs* 2004;28:940–4.
12. Abe Y, Isoyama T, Saito I, et al. Development of mechanical circulatory support devices at the University of Tokyo. *J Artif Organs* 2007;10:60–70.
13. Yambe T, Shiraishi Y, Saijo Y, et al. Quantitative evaluation of the baroreflex sensitivity of an artery. *Scripta Medica* 2008; 81:249–60.
14. Liu H, Saijo Y, Zhang X, et al. Impact of type A behavior on brachial-ankle pulse wave velocity in Japanese. *Tohoku J Exp Med* 2006;209:15–21.

31st Annual International Conference of the IEEE EMBS
Minneapolis, Minnesota, USA, September 2-6, 2009

Estimation of Blood Pressure Variability Using Independent Component Analysis of Photoplethysmographic Signal

Makoto Abe, *Member, IEEE*, Makoto Yoshizawa, *Member, IEEE*, Norihiro Sugita, Akira Tanaka, *Member, IEEE*, Shigeru Chiba, Tomoyuki Yambe and Shin-ichi Nitta

***Abstract*— The maximum cross-correlation coefficient $\rho_{\max}$ between blood pressure variability and heart rate variability, whose frequency components are limited to the Mayer wave-related band, is a useful index to evaluate the state of the autonomic nervous function related to baroreflex. However, measurement of continuous blood pressure with an expensive and bulky measuring device is required to calculate $\rho_{\max}$. The present study has proposed an easier method for obtaining $\rho_{\max}$ with measurement of finger photoplethysmography (PPG). In the proposed method, independent components are extracted from feature variables specified by the PPG signal by using the independent component analysis (ICA), and then the most appropriate component is chosen out of them so that the $\rho_{\max}$ based on the component can fit its true value. The results from the experiment with a postural change performed in 17 healthy subjects suggested that the proposed method is available for estimating $\rho_{\max}$ by using the ICA to extract blood pressure information from the PPG signal.**

I. INTRODUCTION

To estimate the state of the autonomic nervous system related to the baroreflex function, the authors have previously proposed the maximum cross-correlation coefficient $\rho_{\max}$ between blood pressure variability (BPV) and heart rate variability (HRV) in Mayer wave band [1][2]. However, measurement of continuous blood pressure is required to obtain $\rho_{\max}$. Instead of blood pressure, we have attended to measurement of photoplethysmography (PPG) which is an inexpensive, non-invasive, and easily attachable device. The index $\rho_{\max}$ obtained from a feature variable of PPG includes some physiological components other than BPV [3]. Thus, $\rho_{\max}$ obtained from feature variables of PPG does not always correspond to $\rho_{\max}$ from BPV. Therefore, in this study, we have proposed a new method for obtaining $\rho_{\max}$ with BPV-related information obtained from measurement of PPG. In this study, heart rate is calculated from the foot-to-foot-interval (FFI) of the PPG signal, and BPV-related information is obtained from the parameter extracted by using the independent component analysis (ICA). The adequacy of the proposed method was evaluated on the basis of comparison with the conventional method.

M. Abe and M. Yoshizawa are with the Research Division on Advanced Information Technology, Cyberscience Center, Tohoku University, 6-6-05 Aoba, Aramaki, Aoba-ku, Sendai 980-8579, Japan (corresponding author to provide phone: +81-22-795-7130; fax +81-22-263-9163; e-mail: abe@yoshizawa.ecei.tohoku.ac.jp).

N. Sugita is with Graduate School of Engineering, Tohoku University, 6-6-05 Aoba, Aramaki, Aoba-ku, Sendai 980-8579, Japan.

A. Tanaka is with Faculty of Symbiotic Systems Science, Fukushima University, 1 Kanayagawa, Fukushima 960-1296, Japan.

S. Chiba is with Sharp Corporation, 1-9-2 Nakase, Mihama-ku, Chiba 261-8520, Japan.

T. Yambe and S. Nitta are with Institute of Development, Aging and Cancer, Tohoku University, 4-1 Seiryo-cho, Aoba-ku, Sendai 980-8575, Japan.

II. METHODS

A. Maximum cross-correlation coefficient $\rho_{\max}$

Let $u(i)$ and $v(i); i = 0, 1, 2, \ldots$ denote time series data, for example, blood pressure variability (BPV) and heart rate variability (HRV), respectively, sampled with a sampling period $\Delta t = 0.5$s. They are filtered through a band-pass digital filter with a bandwidth between 0.08Hz and 0.12Hz to limit their frequency components to the Mayer wave band. At a certain time point $t = i \cdot \Delta t$[s], a Hamming window with the interval between $t - 60$[s] and $t + 60$[s] is applied to $u(i)$ and $v(i)$. A cross-correlation coefficient $\rho_{uv}(\tau)$ for a lag of $\tau = j \cdot \Delta t$[s]; $j = \ldots, -1, 0, 1, \ldots$ is calculated as follows:

$$\rho_{uv}(\tau) = \frac{\phi_{uv}(\tau)}{\sqrt{\phi_{uu}(0) \cdot \phi_{vv}(0)}} \tag{1}$$

where, $\phi_{uv}(\tau)$ is a cross-correlation function between $u(i)$ and $v(i)$, and $\phi_{uu}(\tau)$ and $\phi_{vv}(\tau)$ are auto-correlation functions of $u(i)$ and $v(i)$, respectively. The maximum cross-correlation coefficient $\rho_{\max}$ and the lag from BPV to HRV $\tau_{\max}$ are defined as

$$\rho_{\max} = \max_{0\text{s} \le \tau \le 10\text{s}} \rho_{uv}(\tau) \tag{2}$$

$$\tau_{\max} = \arg \max_{0\text{s} \le \tau \le 10\text{s}} \rho_{uv}(\tau). \tag{3}$$

In the present study, $\rho_{\max}$ is successively calculated every one second between $t = 60$[s] and $t = T - 60$[s], where T[s] is the end time of the data obtained from an experiment.

B. Independent component analysis (ICA)

The ICA used in our method is described as follows:

1) Let $x_1(k), x_2(k), \ldots, x_m(k)$ be m feature variables extracted from the PPG signal at the k-th beat. Define a feature vector $x(k)$ as $x(k) = [x_1(k), x_2(k), \ldots, x_m(k)]^{\mathrm{T}}$.
2) Let $s_1(k), s_2(k), \ldots, s_n(k)$ be n unknown physiological parameters that are independent of one another at the k-th beat. Define a parameter vector $s(k)$ as $s(k) = [s_1(k), s_2(k), \ldots, s_n(k)]^{\mathrm{T}}$.
3) Assume that the feature vector $x(k)$ is given by a linear combination of $s_1(k), s_2(k), \ldots, s_n(k)$ as follows:

978-1-4244-3296-7/09/$25.00 ©2009 IEEE